CELL BIOLOGY

BioID-based intact cell interactome of the Kv1.3 potassium channel identifies a Kv1.3-STAT3-p53 cellular signaling pathway

Elena Prosdocimi[1]†, Veronica Carpanese[1]†, Luca Matteo Todesca[1], Tatiana Varanita[1], Magdalena Bachmann[1]‡, Margherita Festa[1]§, Daniele Bonesso[1], Mireia Perez-Verdaguer[1], Andrea Carrer[1,2], Angelo Velle[1], Roberta Peruzzo[1]¶, Silvia Muccioli[1]#, Davide Doni[1], Luigi Leanza[1], Paola Costantini[1], Frank Stein[3], Mandy Rettel[3], Antonio Felipe[4], Michael J. Edwards[5], Erich Gulbins[6], Laura Cendron[1], Chiara Romualdi[1], Vanessa Checchetto[1]*, Ildiko Szabo[1]*****

Kv1.3 is a multifunctional potassium channel implicated in multiple pathologies, including cancer. However, how it is involved in disease progression is not fully clear. We interrogated the interactome of Kv1.3 in intact cells using BioID proximity labeling, revealing that Kv1.3 interacts with STAT3– and p53–linked pathways. To prove the relevance of Kv1.3 and of its interactome in the context of tumorigenesis, we generated stable melanoma clones, in which ablation of Kv1.3 remodeled gene expression, reduced proliferation and colony formation, yielded fourfold smaller tumors, and decreased metastasis in vivo in comparison to WT cells. Kv1.3 deletion or pharmacological inhibition of mitochondrial Kv1.3 increased mitochondrial Reactive Oxygen Species release, decreased STAT3 phosphorylation, stabilized the p53 tumor suppressor, promoted metabolic switch, and altered the expression of several BioID-identified Kv1.3-networking proteins in tumor tissues. Collectively, our work revealed the tumor-promoting Kv1.3-interactome landscape, thus opening the way to target Kv1.3 not only as an ion-conducting entity but also as a signaling hub.

INTRODUCTION

Voltage-gated potassium (Kv) channels are a large group of ion channels with wide expression in excitable and nonexcitable cells. Kv channels participate in modulating Ca^{2+} signaling, cell volume, cell cycle progression, adhesion, and apoptosis (*1*). Kv1.3, a member of the *Shaker* Kv1 channel family, harbors six transmembrane segments and the pore region between S5 and S6. Cytoplasmic N- and C-terminal domains play a role in the regulation of K^+ fluxes, but also participate in cellular signaling through protein-protein interactions (*2*) that are only partially elucidated. Kv1.3 is expressed in neurons and in nonexcitable cells, such as immune cells, kidney and colon epithelia, osteoclasts, smooth muscle, testes, and adipocytes (*3*). The channel is emerging as crucial in the context of many severe pathologies ranging from autoimmune to neurodegenerative diseases (*4*–*6*) and cancer (*7*, *8*). The way that the channel links to these pathologies at the molecular level has not yet been fully elucidated (*9*).

Ion channels can take part in large macromolecular complexes that affect their function as well as downstream signaling. These complexes have been characterized mostly by standard biochemical techniques, including pull-down assays. Recently, proximity-dependent labeling techniques have been developed with the aim of overcoming the limitations imposed by antibody-based techniques and the use of detergents. BioID exploits the promiscuous biotin ligase BirA* (*10*, *11*) and does not require detergents. In addition, BioID can detect even weak and transient interactions with proteins proximal to a protein of interest fused in the frame to BirA* [i.e., within a small radius (10 nm)]. After the addition of biotin, BirA* catalyzes covalent biotinylation of proximal proteins. This posttranslational modification is then exploited for subsequent streptavidin-mediated purification and mass spectrometry (MS) to identify interacting proteins. Even if this method represents a cutting-edge tool to study the function of this class of proteins, BioID has only recently been used to identify ion channels interactors just in a few cases (*12*–*14*).

Our objective was to gain in-depth insight into the interactome of Kv1.3 in intact cells. Second, we aimed to decipher the cancer-related pathways regulated by the channel during tumor growth. Several studies have addressed Kv1.3-linked signaling in autoimmune diseases, but possible signaling pathways linking Kv1.3 to cancer just begin to emerge in vitro (*15*, *16*). Kv1.3 is functionally active not only in the plasma membrane but also in mitochondria (*17*–*19*), where it associates with complex I of the respiratory chain (*20*) and mediates apoptosis (*21*). An altered expression and function of Kv1.3 is found in many types of cancer cells (*7*, *22*). A positive correlation was observed between Kv1.3 expression and tumor progression in most cases. *KCNA3* encoding Kv1.3 is the most abundantly expressed *KCNA* gene in skin cutaneous melanoma (SKCM), stomach adenocarcinoma, lung adenocarcinoma, and lung squamous cell carcinoma (*23*). Whether cancer progression is linked to Kv1.3 expression in the cancer cells or in the immune cells of the tumor microenvironment awaits clarification (*23*).

[1]Department of Biology, University of Padova, Padova, Italy. [2]Department of Biomedical Sciences, University of Padova, Padova, Italy. [3]EMBL, Heidelberg, Germany. [4]Molecular Physiology Laboratory, Department de Bioquímica i Biomedicina Molecular, Institut de Biomedicina (IBUB), Universitat de Barcelona, Barcelona, Spain. [5]Department of Surgery, University of Cincinnati, Cincinnati, OH, USA. [6]Department of Molecular Biology, University of Duisburg-Essen, Essen, Germany.
*Corresponding author. Email: ildiko.szabo@unipd.it (I.S.); vanessa.checchetto@unipd.it (V.C.)
†These authors contributed equally to this work.
‡Present address: Dana Faber Cancer Institute, 450 Brookline Avenue, Boston, MA 02215, USA.
§Present address: Institute of Biophysics, CNR, Via De Marini, 6 16149 Genova, Italy.
¶Present address: University of California, Berkeley, 175 Li Ka Shing Center #3370, Berkeley, CA 94720-3370, USA.
#AUSL di Reggio Emilia, via Amendola 2, 42122 Reggio Emilia, Italy.
**These authors contributed equally to this work.

In our study, in addition to defining the Kv1.3 interactome using BioID, we performed validation of functional interactions with some of the identified partners. To this end, we generated two stably depleted Kv1.3 melanoma cell lines, revealing substantial differences between Kv1.3 KD and wild-type (WT) melanoma cells in gene expression and cell behavior in vitro, as well as tumor growth and signaling cascades in vivo. Thus, our study uncovers a previously unidentified Kv1.3 channel integrative network and a crucial role of Kv1.3 for in vivo tumorigenesis. These results may prompt the development of potential cutting-edge therapeutics.

RESULTS

Expression of Kv1.3 in combination with BirA* does not alter channel localization and functionality

The cytoplasmic N and C termini of Kv1.3 can adopt different conformations and possibly interact with different partners; therefore, BirA* was fused either to the N or to the C terminus of the channel yielding BirA*-tagged baits. BirA* sequence corresponds to BirAR118G, a promiscuous mutant biotin ligase that can be exploited for BioID (*24*). Human embryonic kidney (HEK) 293 cells are widely used as a model to define Kv partners and for application of BioID to ion channels, such as Kir2.1 (*14*). The BioID experimental workflow is illustrated in fig. S1.

To map the Kv1.3 interactome, we first generated two independent HEK293 cell lines stably expressing Myc-BirA*-Kv1.3 (Fig. 1A) and a cell clone expressing only Myc-BirA* without the channel protein (BioID-only), as a control. Furthermore, we used parental HEK293 cells as a negative control, as reported in (*25*) (Fig. 1B). Next, we confirmed the expected prevalent localization of Myc-BirA*-Kv1.3 to the plasma membrane (Fig. 1C) by immunofluorescence staining using specific antibodies against Myc and PMCA as a PM marker. Similar results were obtained with a second, independent clone (fig. S2A). A part of Kv1.3 is targeted to mitochondria in HEK293 cells, as shown by colocalization of Kv1.3-yellow fluorescent protein (YFP) with Mitotracker Red (fig. S2B). Given that BirA*, which is an enzyme with a molecular weight of 33 kDa, a priori could alter the biophysical properties of Kv1.3, we performed whole-cell patch-clamp experiments and revealed a channel activity with the classical biophysical properties of Kv1.3, namely, voltage dependence and inactivation kinetics (Fig. 1D; for comparison, see endogenous Kv1.3 current in fig. S2C). Thus, BirA*-Kv1.3 was correctly localized and functional in the plasma membrane. Subsequently, we obtained evidence that upon the addition of exogenous biotin, biotinylation occurred in the proximity of Kv1.3, observing a nearly complete overlap of streptavidin–Alexa Fluor 488 conjugate that strongly binds all biotinylated proteins and anti-Myc antibody, indicating the presence of Kv1.3 (Fig. 1E). The specificity of biotinylation as well as its efficiency was confirmed by Western blot: In the BioID-only control (Myc-BirA*), we visualized proteins that showed affinity for BirA* and were biotinylated as revealed by horseradish peroxidase (HRP)–coupled streptavidin. The addition of biotin triggered instead a strong biotinylation of several proteins in the sample expressing the Myc-BirA*-Kv1.3 construct (Fig. 1F). Next, we determined a suitable labeling time that yielded sufficient biotinylated material, without inducing toxicity due to chronic biotinylation of endogenous proteins and saturation of proximal labeling sites. As shown in Fig. 1G, a time-dependent biotinylation occurred, reaching an elevated level after 24 hours. In the absence of exogenously added biotin, no increase in biotinylation was observed as a function of time (fig. S2D).

The same experiments were also performed with cells expressing BirA* in fusion at the C terminus of the channel (Kv1.3-BirA*-HA) (fig. S3A). The fusion protein, when stably expressed in HEK293 cells, reached the plasma membrane (fig. S3, B and C) and gave rise to voltage-dependent Kv1.3 activity (fig. S3D). In this case, inactivation kinetics were slightly slower but compatible with other reports showing Kv1.3 activity expressed in HEK293 cells (*26*). Biotinylation was observed in correspondence to channel location within cells as detected by immunofluorescence labeling (fig. S3E) and Western blot (fig. S3F). Biotinylation occurred in a time-dependent manner in intact cells (fig. S3G). As a control, BirA*-HA was used in the above experiments (BioID-only control) (fig. S3F).

BioID detects Kv1.3-interacting proteins

We first analyzed the interactome of independent clones of BirA* fused to either the N terminus or the C terminus of the channel. In each clone, expressing Kv1.3 in fusion with the tagged biotin ligase (named Myc-BirA*-Kv1.3 #1 and Myc-BirA*-Kv1.3 #2 for the two clones where the biotinylating enzyme BirA* fused to the N terminus of the channel protein, and Kv1.3-BirA*-HA for the clone where BirA* fused to the C terminus of the channel), a strong biotinylation was observed after incubation of cells with biotin (see Fig. 1, F and G, and fig. S3, F and G). In parallel, analysis of BirA*-only tagged controls that express the biotin ligase only (named Myc-BirA* and BirA*-HA, BioID-only samples) (Fig. 1F and fig. S3F) allowed us to identify endogenously biotinylated proteins. An additional control was performed in cells lacking the expression of any BioID ligase (named parental HEK293).

Whole-cell extracts expressing various bait proteins were prepared from cells cultured in the absence or presence of biotin (indicated as "minus" and "plus" in Fig. 1F and fig. S3F). After cell lysis, the biotinylated proteins were purified using streptavidin beads and analyzed by MS.

We used multiplexed quantitative MS using tandem mass tag (TMT) labeling to assess proximity-dependent biotinylation in a proteome-wide fashion. After digestion of the proteins into peptides, we chemically tagged the peptides with isotopically distinct TMT labels. This enabled us to quantify the relative abundance of each protein across the samples as previously described (*27*, *28*). An overview of the normalized TMT reporter ion intensities (see Materials and Methods for details) for each condition and replicate is shown in fig. S4A.

To evaluate the enrichment of biotinylated proteins following biotin treatment (plus versus minus conditions), we tested normalized raw TMT reporter ion intensities for differential abundance using a moderated *t* test. Hit proteins (table S1) had a ratio greater than 2 [log2 fold change (FC) > 1] and a false discovery rate (FDR) less than 0.05. We identified 465, and 507 and 398 proteins for the C-terminal and the two N-terminal clones, respectively (see volcano plots in fig. S4B). A substantial part of the BioID-identified Kv1.3 partners were also identified by classical coimmunoprecipitation assay exploiting the Myc-Trap system using Myc-tagged Kv1.3 (fig. S4C and table S2). Sixty-three proteins identified in our assays were located in mitochondria (highlighted in yellow in tables S1 and S2), as identified using Mitocarta2.0 (*29*), in accordance with the previously reported location of Kv1.3 in this organelle (*21*).

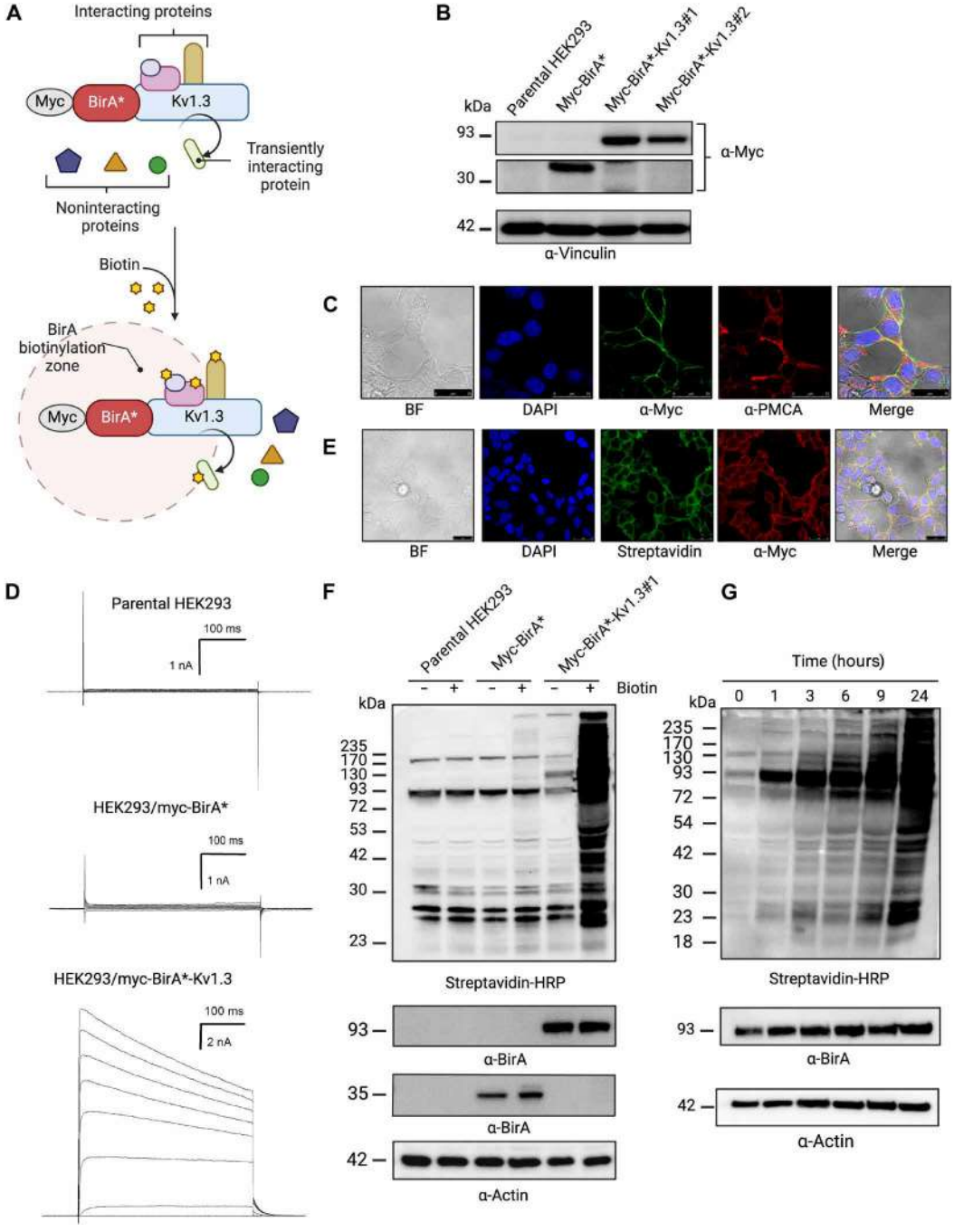

Fig. 1. Characterization of cells stably expressing myc-BirA*-Kv1.3 fusion proteins. (**A**) Cartoon of myc-BirA*-Kv1.3. BirA* is shown fused to the Kv1.3 N-terminal end. BirA* converts exogenously added biotin to highly reactive labile biotinyl-5′-AMP, allowing it to react with primary amines on vicinal/interacting proteins. The labeling radius is around 10 nm. (**B**) HEK293 cells were stably transfected with myc-BirA*-Kv1.3 or myc-BirA*. Following SDS-PAGE of cell lysates, myc-BirA*-Kv1.3 or myc-BirA* proteins were detected with anti-BirA. Fifty micrograms of protein per lane was loaded as indicated: parental HEK293 cells (control, untransfected cells); HEK293 cells transfected with the empty vector (myc-BirA* vector); two independent clones expressing myc-BirA*-Kv1.3. Vinculin: loading control. (**C**) Immunofluorescence analyses of HEK293 cells stably expressing myc-BirA*-Kv1.3. Localization of BirA*-fusion proteins detected at the PM with fluorescently labeled anti-myc (green). The PM PMCA (red) colocalize with the Kv1.3 fusion protein (see merge). DNA is labeled with DAPI (blue). Scale bar, 25 μm. A representative image of three independent experiments is shown. (**D**) Kv1.3 currents elicited by applying a train of depolarizing potentials in 20 mV stepwise increases up to +70 mV from a −70 mV holding potential ($n = 3$ for each). (**E**) Confocal images of HEK293 cells stably expressing myc-BirA*-Kv1.3 (clone #1) after 24 hours of incubation with exogenous biotin (50 μM). Myc-BirA*-Kv1.3 was detected with anti-myc (red) and biotinylated proteins with fluorescently labeled streptavidin (green). Scale bar, 25 μm. (**F**) HEK293 cells stably expressing myc-BirA*-Kv1.3, or parental and empty vector controls, were analyzed 24 hours after biotinylation induction with (+) or without (−) exogenous biotin supplementation. Biotinylated proteins were detected with streptavidin-HRP. Middle: the Kv1.3 fusion protein detected with anti-BirA. Bottom: Anti-actin was protein loading control ($n = 3$ independent experiments). (**G**) As in (F) in the presence of 50 μM biotin at different time points ($n = 3$). Loading control of the same blot is shown.

Bioinformatic analysis reveals previously unidentified Kv1.3-linked signaling pathways

A total of 378 proteins were identified in BioID as hits (compared to the respective nonbiotin controls) in all three clones (referring to both the C and N termini), 87 proteins in two clones and 62 proteins in a single clone only. Overlap of the set of proteins from the three clones is shown in fig. S4D. None of these 527 hits were enriched in the biotin conditions of the BioID-only samples or the nontransfected HEK293 cells (fig. S4E), indicating that all 527 proteins were biotinylated due to proximity to Kv1.3 in fusion with BirA*. Figure S4E shows the log2 ratios of the biotin versus nonbiotin (plus/minus) conditions in the N terminus and C terminus compared to the control and in the N terminus versus the C terminus. These graphs indicate a number of hits (red) that are well distinguishable when considering the enriched biotinylated proteins found in cells expressing BirA* in fusion with Kv1.3 compared to those found in controls (BioID-only, HEK293), where some endogenously biotinylated proteins are present, as expected. There were no differences between the two N-terminal clones, while a dozen of proteins were different between the N-terminal and C-terminal clones (myc-BirA*-Kv1.3 and Kv1.3-BirA*-HA, respectively).

More specific bioinformatic analyses identified molecular pathways linked to the Kv1.3 interactome, at both the N terminus and the C terminus (527 proteins). The whole dataset of proteins identified as hits was interfaced with the KEGG (Kyoto Encyclopedia of Genes and Genomes) and Reactome databases and classified using Gene Ontology (GO) categories, extracting information about cell functions and pathways activated and connected to Kv1.3. The gene set enrichment analyses performed on identified hits using the biological process ontology indicated an enrichment of 270 categories. Thus, we found proteins implicated in the positive regulation of cell junction assembly, regulation of actin filament–based process, actin filament organization protein, localization to cell periphery, protein localization to plasma membrane, regulation of protein-containing complex assembly, regulation of supramolecular fiber organization, regulation of guanosine triphosphatase (GTPase) activity, regulation of actin cytoskeleton organization, and cell-cell junction organization (fig. S5A) for top enriched terms. The scatterplot of the entire list of significantly enriched GO terms after the redundancy reduction obtained by semantic similarity analysis is shown in fig. S6. The GO terms are reported in a two-dimensional space derived by applying multidimensional scaling to a matrix of the GO terms' semantic similarities. The names of the most significant GO term clusters are reported. GO term clusters closed in the two-dimensional space are semantically similar. The size of the dots is proportional to the size of the category (the larger the dots are, the more general is the term).

Analysis of molecular functions (fig. S5B) for top enriched terms (and fig. S7A for the treemap visualization of the entire enriched list) also showed enrichment in cadherin binding, actin binding, GTPase regulator activity, GTPase activator activity, GTPase binding, small GTPase binding, nucleoside-triphosphatase regulator activity, molecular adaptor activity, phospholipid binding, tubulin binding, actin filament binding, and phosphatidylinositol binding. Most of the Kv1.3-interacting proteins were localized to cell-cell junctions, focal adhesions, cell-substrate junctions, and cell leading edges (fig. S5C) for the top enriched terms (and fig. S7B for the treemap visualization of the entire enriched list).

In addition, pathway analysis of the Reactome database (Fig. 2A) uncovered (with an FDR < 0.1) the physical proximity of Kv1.3 to proteins related to different cellular signaling pathways, including the apoptotic execution phase, apoptotic cleavage of cell adhesion proteins, Rho GTPase cycle, Rhoh GTPase cycle, RhoBtb GTPase cycle, cell-cell communication, signaling by mesenchymal-epithelial transition, activation of RAC1. and signaling by anaplastic lymphoma kinase in cancer. The right part of Fig. 2A reports the single interactors grouped into cancer-relevant pathways.

The results of the KEGG pathway analysis (Fig. 2, B and C, for the 20 enriched pathways) revealed that Kv1.3 is intimately associated with various sites within the cell [including the focal adhesion (fig. S8), adherens, and tight junctions (not shown)] and with various pathways, including protein processing in the endoplasmic reticulum (fig. S9), the Erbb signaling pathway (fig. S10), proteoglycans in cancer (fig. S11), Hippo pathway (fig. S12), and regulation of the actin cytoskeleton. In all KEGG pathways, the color of the interacting protein is correlated with its log2 FC value, revealing that biotinylation of these Kv1.3-adjacent proteins occurred with high frequency, suggesting a rather strong interaction when reaching high values. The complete list of identified enriched GO terms and pathways is available in table S3.

Similar results were also obtained when the N-terminal and C-terminal interactomes of Kv1.3 were separately analyzed. However, some differences could be observed, as illustrated in fig. S13 (A and B) for, respectively, GO categories and Reactome pathways. These experiments highlight interesting differences, such as, for example, specific interaction with proteins harboring phosphatase activity, with those of endosomal sorting complex required for transport, and those involved in phosphoinositide 3-kinase/AKT serine-threonine protein kinase (PI3K/AKT) signaling at the C terminus of the channel protein. Instead, members of the MAPK (mitogen-activated protein kinase) family signaling cascade are found in BioID of the N terminus–linked BirA*, allowing future identification of specific regions of the channel that are involved in these specific signaling hubs.

Last, unbiased hierarchical clustering was performed based on the log2-fold change of each cell line sample, compared to HEK293 cells without the addition of biotin. The cluster number is shown to the right of the heatmap (Fig. 2D), and for each cluster, the result of the GO enrichment analysis is indicated in relation to molecular function (Fig. 2E), biological processes (fig. S14A), and the cellular compartment (fig. S14B).

Kv1.3 is linked to cancer-related pathways

Because our KEGG analysis highlighted many cancer-related pathways [e.g., Erbb2, signal transducer and activator of transcription 3 (STAT3), SHP2, and epidermal growth factor receptor (EGFR)], we aimed to validate our findings in a tumoral context. Expression of Kv1.3-encoding *KCNA3* in SKCM, one of the most aggressive cancers that arise from transformed melanocytes, is higher in tumoral tissues with respect to nontumoral tissues according to the The Cancer Genome Atlas public database (fig. S15A) and *KCNA3* transcript level slightly increases from stage 0 to stage I (fig. S15B).

The B16F10 mouse melanoma line that expresses Kv1.3 (*30*) is widely used to study SKCM tumorigenesis [e.g., (*31*)]. Therefore, we first generated two independent stable knockout B16F10 melanoma lines using the CRISPR-Cas9 technology (*32*, *33*), which is suitable for down-regulating ion channel expression in cancer cells [see, e.g., (*34*)]. Two knockdown clones (KD clones) (fig. S16) in which lack of

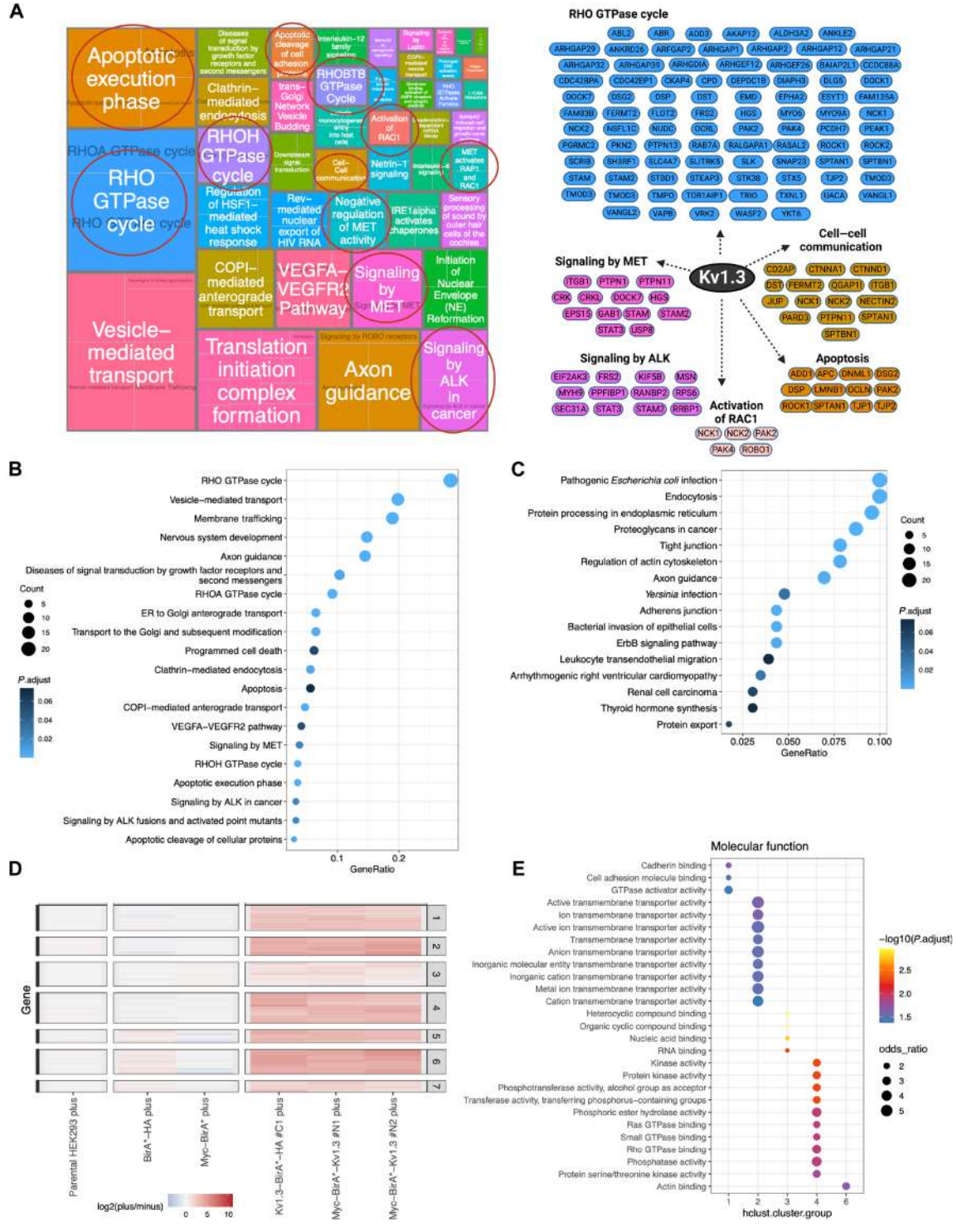

Fig. 2. Pathway analysis of the interacting proteins. (**A**) Treemap of the significantly enriched Reactome pathways. Each rectangle is a significant GO term that is joined into clusters of semantically related terms, visualized with different colors. The size of the rectangles reflects the *P* value of the GO term in cluster: Larger rectangles indicate higher significance. The genes belonging to the clusters highlighted with red circles were used to draw the schematic representation of the Kv1.3 interactome reported in the right part. (**B** and **C**) Dot plots reporting the top 20 significantly enriched Reactome pathways (B) and the 16 most significant KEGG pathways (C) obtained using the 527 hit proteins. On the *x* axis, the ratio between the number of hit proteins belonging to the pathway (count) and the total size of the pathway is reported. The dimension of the dot indicates the count (the larger the dot, the higher the count), and the color of the dot represents the adjusted *P* value. (**D**) Cluster analyses of hit proteins obtained using log2 FC of the plus/minus samples. (**E**) Dot plots reporting the top 20 significantly enriched GO terms for molecular function. The dimension of the dot represents the odds ratio and the color denotes the adjusted *P* value.

Kv1.3-encoding *KCNA3* was confirmed by polymerase chain reaction (PCR) and bands reacting with anti-Kv1.3 antibody were barely detectable in Western blot (Fig. 3A) were used for further studies.

Given the role of K^+ channels, including Kv1.3, in promoting the proliferation of cancer cells (*1*), we first tested whether knockdown of Kv1.3 affected cellular proliferation. The clones showed a reduced proliferation rate (Fig. 3B). Next, we investigated the clonogenic ability of Kv1.3 KD clones in vitro. The area covered by each colony showed a significant decrease (Fig. 3C). In agreement with our recent work showing an altered mitochondrial network in the absence of Kv1.3 in adipocytes (*35*), we observed that the Kv1.3 KD melanoma cells harbored swollen mitochondria and a fragmented mitochondrial network (Fig. 3D) and displayed higher mitochondrial reactive oxygen species (ROS) level compared to WT (Fig. 3E). The observed mitochondrial fragmentation may contribute to the reduced proliferation and colony formation in melanoma [e.g., (*36*, *37*)]. Ion channels and transporters may also affect tumor behavior by regulating cancer cell migration (*38*). The impact of the lack of Kv1.3 on B16F10 cell migration was assessed in vitro in wound healing assay, showing that the KD cells migrated slower than WT cells (Fig. 3F).

Next, we assessed the activation state of some cancer-relevant pathways related to Kv1.3. For example, cyclin D1 is stabilized by the absence of the channel in B16F10 melanoma cells in accordance with our previous findings showing that knockdown of Kv1.3 in preadipocytes resulted in delayed G_1-S phase transition as indicated by a sustained increase in cyclin D1 levels (*35*) (fig. S17).

We identified an unexpected partner of Kv1.3 revealed by BioID as well as classical coimmunoprecipitation, namely, the transcription factor STAT3 [see table S2 (G8JLH9)], whose decreased phosphorylation at Ser^{727} is associated with a diminished tumorigenic phenotype of B16F10 cells, while phosphorylation at Y705 has been linked to stem cell proliferation (*39*). First, to confirm interaction between Kv1.3 and STAT3 in intact cells, we performed the proximity ligation assay (PLA) and revealed the PLA signal both at the level of the PM and intracellularly, in HEK293 (Fig. 4A and fig. S18, A and D, for enlarged images) and in KD B16F10 cells that were transfected with Kv1.3 in fusion with YFP (Fig. 4A and fig. S18, B and D). Furthermore, the PLA signal was also observable at the level of mitochondria in cells expressing a mitochondria-targeted version of Kv1.3 (fig. S18D). The W386F pore-dead mutant of the channel was able to interact equally with STAT3 when expressed in the KD B16F10 cells (Fig. 4A and fig. S18C).

In addition, classical IP also revealed a detectable interaction between the two proteins (Fig. 4B). In B16F10 cells as well as in SK-MEL28 melanoma cells, KD for Kv1.3 reduction in both the expression level and activation of STAT3 (by Ser^{727} phosphorylation) was detected (Fig. 4C), in accordance with the known phosphorylation-induced stabilization of STAT3. Given that Kv1.3 is functional both in the plasma membrane and in mitochondria (mitoKv1.3) and PLA revealed STAT3-Kv1.3 at both locations, we aimed to understand (i) whether inhibition of the former or latter population is sufficient to decrease STAT3 activation and (ii) whether inhibition of the channel activity or lack of Kv1.3 protein is required to exert an effect on STAT3 activation. To this end, we exploited membrane-impermeant toxin inhibitors Margatoxin (Mgtx) and *Stichodactyla* toxin (Shk) or the mitochondria-targeted Kv1.3 inhibitor (3-(4-(4-((7-oxo-7H-furo[3,2-g]benzopyran-4-yl)oxy)butoxy)phenyl)propyl)triphenyl phosphonium iodide (PAPTP) (*40*). Neither Mgtx nor Shk was able to dampen STAT3 activation, while application of PAPTP was sufficient to decrease STAT3 phosphorylation and stability not only in B16F10 cells (Fig. 4D) but also in COLO357 pancreatic ductal adenocarcinoma cell line, previously shown to express mitoKv1.3 (*41*) (Fig. 4E). Altogether, these results suggest that the channel activity/presence of mitoKv1.3 is required to maintain activation of this crucial protumorigenic transcription factor even in different tumor types, while blocking the channel at the PM is not sufficient to abolish STAT3 activation.

Mitochondria-located Kv1.3 has been linked to apoptosis (*9*) and the p53 tumor suppressor is a critical regulator of apoptosis in B16F10 cells (*42*). A recent study showed that inactivation of STAT3 enhanced p53 expression and activation, and this, in turn, contributed to a decrease in total STAT3 protein levels (*43*); therefore, we explored the effect of channel deletion/inhibition on p53 expression. Notably, p53 level was substantially increased upon deletion of Kv1.3 in B16F10 cells (Fig. 5A), upon silencing of the channel in SKMEL28 cells (fig. S19A and Table 1), and upon inhibition of mitoKv1.3 with PAPTP (Fig. 5B), indicating stabilization of this important tumor suppressor. Given that enhanced p53 phosphorylation at S392 is associated with mitochondrial translocation and proapoptotic activity of p53 (*44*) and was shown to increase p53 tetramerization, stability, and the tumor-suppressing activity of p53 (*45*), we tested whether p53 S392 is increased in cells lacking Kv1.3. As shown in Fig. 5A, lack of the channel was able to trigger phosphorylation of p53. PAPTP also enhanced phosphorylation of p53 at S392 (Fig. 5C). As PAPTP induces mitochondrial ROS release (*41*), we preincubated the cells with the mitochondrial ROS scavenger MITOTEMPO and observed that this treatment prevented the effect of PAPTP on p53, both on the total p53 and on the phosphorylated forms (Fig. 5C). PAPTP did not exert effects on p53 stabilization or STAT3 activation in the Kv1.3 KD lines, indicating specificity of its action via Kv1.3 (fig. S19).

Our data thus suggest a previously unidentified Kv1.3-STAT3-p53 axis in cancer cells. To further explore this signaling axis, we expressed Kv1.3 in HEK293 cells (that do not endogenously express the channel; see Fig. 1C). Upon expression of Kv1.3 solely, STAT3 level and STAT3 phosphorylation at both S727 and Y705 increased, while p53 stabilization decreased (Fig. 5D). STAT3 activation and p53 stabilization strictly depended on the presence of the channel also in the tumoral context, as indicated by rescue upon the re-expression of Kv1.3 in Kv1.3 KD B16F10 cells (Fig. 5E). Furthermore, silencing of STAT3 in B16F10 cells resulted in a clear increase in p53 level, in accordance with the recently proposed STAT3-p53 connection (Fig. 5F). The effect of PAPTP was abolished on p53 stabilization in cells that were silenced for STAT3 (Fig. 5F), further indicating that Kv1.3 modulation exerts its effect on p53 via STAT3.

STAT3 harbors Src homology 2 (SH2) domains (*46*) and thus may directly bind to the SH2 recognition site of the channel (fig. S20A). The minimal consensus sequence that is recognized by STAT3 SH2 in the target proteins is $Y(PO_3H_2)xxQ$, shortly pYxxQ, where X might be any residue with a preference toward lipophilic or basic amino acids (*47*). Previous docking studies (*48*) based on gp130 phosphopeptide (pYLPQ), or the STAT3-derived phosphopeptide pY705 (corresponding to the STAT3 pY motif responsible for dimerization), demonstrated that phosphotyrosine pY and glutamine in position pY + 3 tightly anchor the consensus peptide to two adjacent and highly conserved STAT3 pockets (fig. S20B), establishing a network of hydrogen bonds and salt bridges with the phosphate group

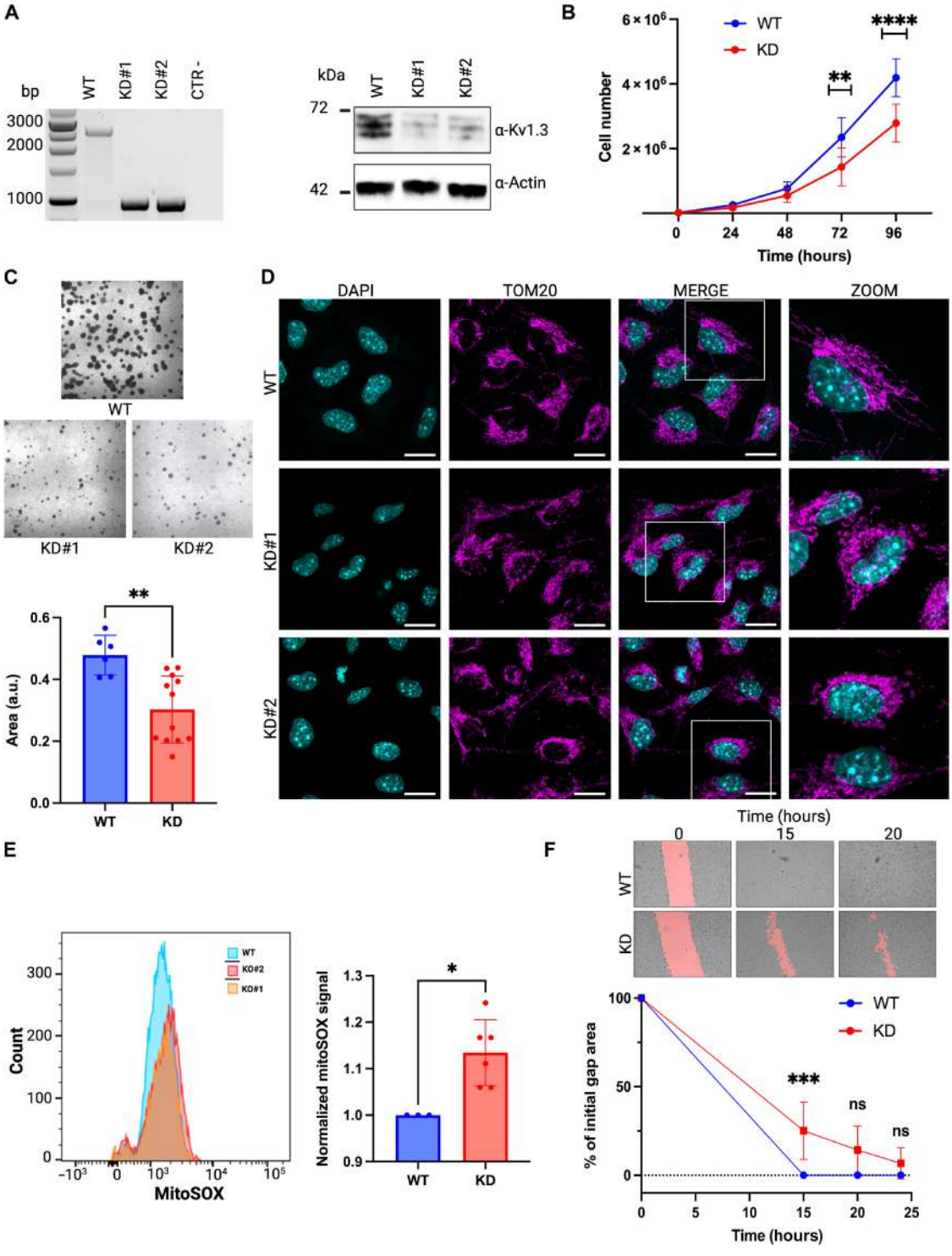

Fig. 3. Generation and characterization of Kv1.3 KD B16 F10 cells. (**A**) Left: PCR performed with the primers F1 and R2b on the B16F10 clones: the expected band for the WT is 2709 bp and the deleted band is expected to be approximately 1000 bp. The positive control was the B16F10 WT, and the negative control was water. Right: Western blot of WT and two independent KD lines ($n = 3$). Protein products with slightly different MWs are observable and are due to glycosylation [e.g., (*95*)]. (**B**) Proliferation rate of B16F10 cells and the Kv1.3 KD clones ($n = 4$, two-way ANOVA, $P < 0.05$). Parental B16F10 and Cas9-transfected cells displayed the same proliferation rate (not shown, $n = 3$). (**C**) Colony formation assay ($n = 6$ for each line) (one-way ANOVA, $P < 0.05$). The number and the dimension of colonies were measured with ImageJ (**D**) Representative confocal images of WT and Kv1.3 KD #1 and #2 B16F10 cells showing a fragmented mitochondrial network. Cells were stained for mitochondrial marker TOM-20 (magenta) and DAPI (cyan). Scale bars, 5 μm. (**E**) Mitochondrial ROS release was measured using Mitosox and FACS analysis. A representative experiment is shown on the left, while the right panel reports values normalized on WT cells' Mitosox fluorescence signal. (**F**) Wound healing assay. Quantification as % of initial gap area ($n = 4$) (two-way ANOVA, $P < 0.05$). Images were analyzed with ImageJ and applied.

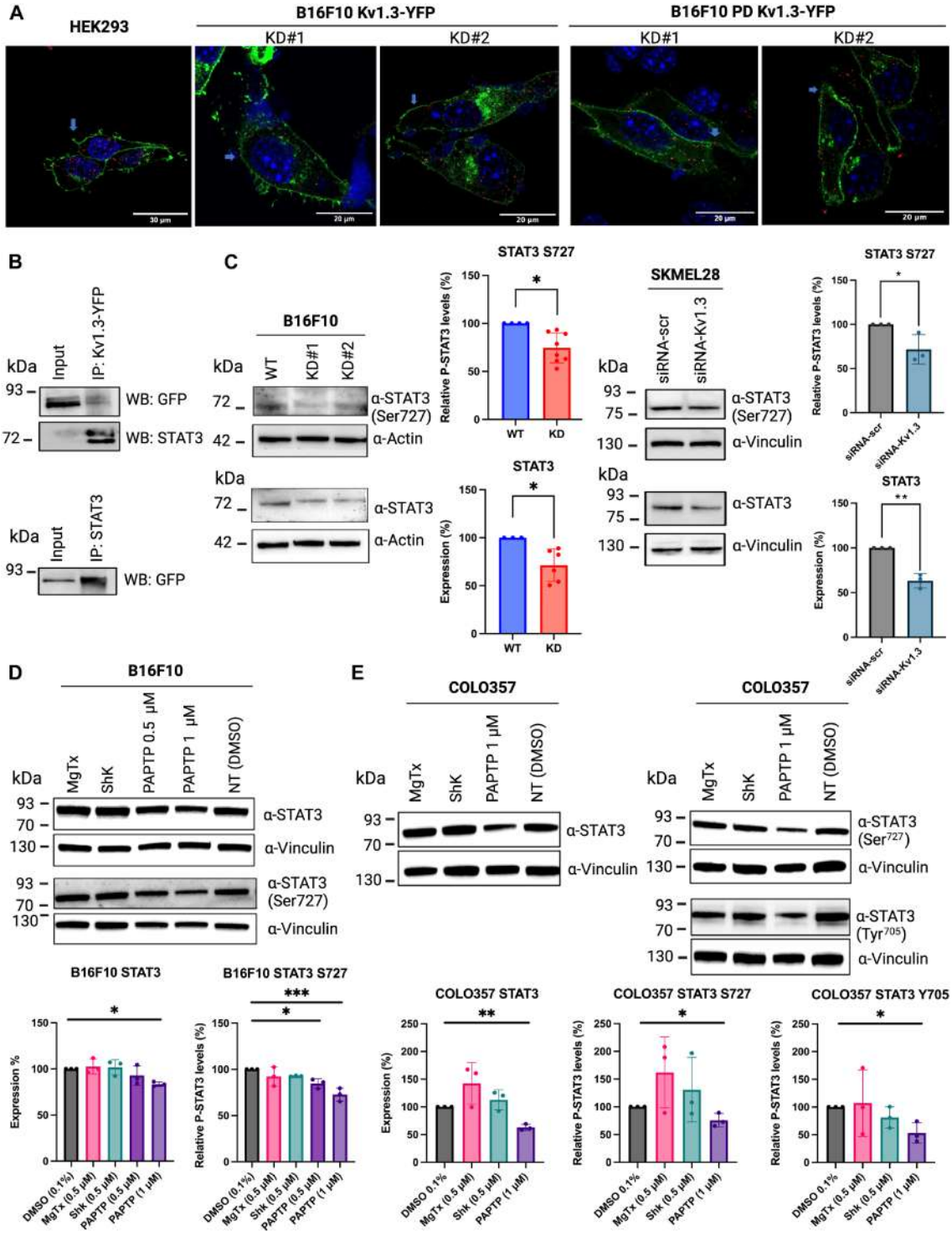

Fig. 4. Kv1.3 expression affects STAT3 signaling. (**A**) Representative confocal images of HEK cells and Kv1.3 KD #1 and #2 B16F10 cells transfected with either Kv1.3-YFP WT or PD Kv1.3-YFP (green), in which proximity ligation assay (PLA) was performed (red). Cells were also stained with DAPI (blue). (**B**) Kv1.3 coimmunoprecipitates with STAT3 in B16F10 KD #1 expressing Kv1.3-YFP. Immunoprecipitation for Kv1.3-YFP and STAT3, immunoblotted for STAT3 and GFP. (**C**) Analysis of expression and phosphorylation levels of STAT3 (Ser^{727}) and total STAT in B16F10 WT and two B16F10 Kv1.3 KD clones. Analysis of expression and phosphorylation levels of STAT3 (Ser^{727}) and total STAT in SKMEL28 WT (scramble, scr) and KD clones (siRNA-Kv1.3). (**D**) Analyses of Ser^{727} STAT3 phosphorylation level and of total STAT3 expression level after treatment with Margatoxin (Mgtx, 0.5 μM) and Stichodactyla toxin (Shk, 0.5 μM) and the mitochondria targeted Kv1.3 inhibitor PAPTP (0.5 and 1 μM) in B16F10 cells. Vinculin was used as the loading control. (**E**) Analyses of Ser^{727} and Tyr^{705} STAT3 phosphorylation level and of total STAT3 level after treatment with Margatoxin (0.5 μM) and Stichodactyla toxin (0.5 μM) and PAPTP (1 μM) in COLO357 cells (all blots have $n = 3$; $^{*}P < 0.05$; $^{**}P < 0.001$; $^{***}P < 0.0001$).

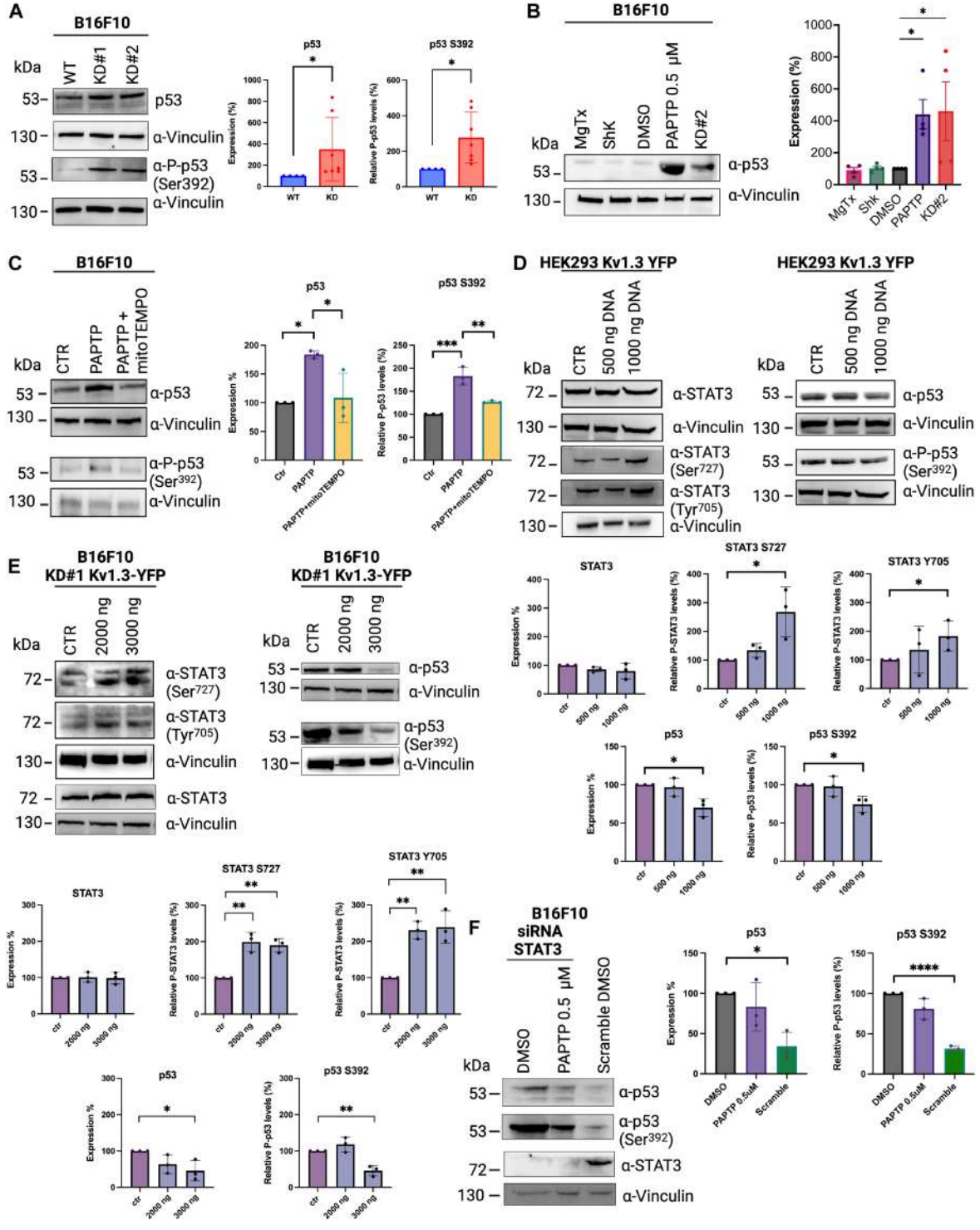

Fig. 5. The Kv1.3-STAT3-p53 axis. (**A**) Analysis of expression and phosphorylation levels of p53 (Ser^{392}) and total p53 in B16F10 WT and two B16F10 Kv1.3 KD clones. (**B**) Analysis of p53 expression level after treatment with Margatoxin (Mgtx, 0.5 μM) and Stichodactyla toxin (Shk, 0.5 μM) and the mitochondria targeted Kv1.3 inhibitor PAPTP (0.5 and 1 μM) in B16F10 cells. Vinculin was used as the loading control (30 μg of protein from cell lysates per lane, $n = 3$). (**C**) Analysis of expression and phosphorylation levels of p53 (Ser^{392}) and total p53 in B16F10 WT treated with PAPTP (0.5 μM) and mitoTEMPO (mT, 100 nM). (**D**) Analysis of expression and phosphorylation of p53 and STAT3 levels in HEK293 cells expressing Kv1.3-YFP. (**E**) Analysis of expression and phosphorylation of p53 and STAT3 levels in B16F10 KD cells expressing Kv1.3-YFP. For (D) and (E), see description of the procedure in Materials and Methods. (**F**) Analysis of expression and phosphorylation of p53 levels in B16F10 silenced for STAT3 ($n = 3$ for all blots; $^{*}P < 0.05$; $^{**}P < 0.001$; $^{***}P < 0.0001$).

Table 1. Primers used for qRT-PCR to detect Kcna3 transcript levels.

m*Tbp* (for)	GCAGTGCCCAGCATCACTAT
m*Tbp* (rev)	GCCCTGAGCATAAGGTGGAA
m*Kcna3* (for)	CCCCAGTAAAGCCACCTTCT
m*Kcna3* (rev)	CTGCCCATTACCTTGTCGTT

(pY pocket). Given these premises, we analyzed by docking analysis the phosphotyrosine sites at the N and C termini of Kv1.3 and observed that the phosphorylated sequence pY111YYQ114 might define a consensus for the STAT3 SH2 domain. Our docking results against the full-length STAT3 monomer [Protein Data Bank (PDB): 6NJS and 6NUQ; HPEPDOCK 2.0 server (*49*)] of a five–amino acid–long phosphopeptide, centered on pY111 residue of Kv1.3, suggest a clear propensity of this motif to cluster within the STAT3 SH2 binding pocket (fig. S20C). Analysis of binding pose with the highest scores evidenced a large contact surface of about 480 $Å^2$ and a highly conserved placement and interactions peculiar to STAT3 binders and analogous to Y705 STAT3 dimerization motif (PDB: 6QHD) or the peptidomimetic prodrug compound SI109 (PDB: 6NUQ; fig. S20, B and D) (*50*). We wondered whether STAT3 inhibitors may alter channel activity. NSC 74859 that interacts with the DNA binding domain of STAT3 did not alter channel activity in Jurkat cells that endogenously express Kv1.3 and STAT3 (fig. S21).

To gain a more general insight into the consequences of Kv1.3 deletion, the WT and Kv1.3 KD clones were subjected to RNA sequencing (RNA-seq) analysis, revealing a differential expression of 2939 (KD #1) or 3525 (KD #2) transcripts compared to the control cells (table S4). The heatmap of the top 100 most variable genes is shown in Fig. 6A. Analysis of these data revealed that in both clones, the most prominent GO terms associated with the changes refer to ribonucleoprotein complex biogenesis, ncRNA metabolic processes, ribosome biogenesis, and mRNA binding (figs. S22 and S23). rRNA processing was also found to be most differentially present according to Reactome (figs. S24 and S25). All these processes were down-regulated in the Kv1.3 KD clones with respect to the control B16F10 cells. Regarding organelle-specific alteration, surprisingly, the most differentially expressed transcripts were linked to lytic vacuoles and lysosomes in addition to mitochondria (in accordance with the mitochondrial localization of Kv1.3) and the actin cytoskeleton (figs. S26 and S27).

KEGG pathway analysis confirmed the involvement of Kv1.3 in the modulation of ribosome biogenesis in eukaryotes (down) and of lysosome function (up) (figs. S28A and S29A and table S5). In addition, this analysis highlighted an unexpected link between Kv1.3 and steroid biosynthesis; in particular, lack of Kv1.3 led to enhanced expression of genes linked to this metabolic pathway (figs. S28B and S29B).

Although in none of the KD lines was *Tp53* up-regulated at the transcript level, the expression of several p53 transcriptional target genes was enhanced, in accordance with the increased phosphorylation and stabilization of p53 in the KD lines. Namely, we observed an increase in the expression of *Tp53inp1* (tumor protein p53-inducible nuclear protein 1, also named "stress-inducible protein"), *Tp53inp2, Trp53cor1* (tumor protein p53 pathway corepressor 1), and the *Cdkn1a* gene encoding p21 that blocks cell cycle progression at the G_1-S phase (Fig. 6B). Further players involved in cell cycle progression regulation are also up- or down-regulated in the cells lacking Kv1.3 (Fig. 6B). These results are in accordance with increased p53 phosphorylation and cyclin D1 expression as shown above. In agreement with activation of p53, the expression of proapoptotic *Caspase 8* and *Bad* mRNA was also increased along with other factors promoting apoptosis in both clones lacking Kv1.3, while the expression of anti-apoptotic players decreased (Fig. 6C). Activation of p53 is also linked to metabolic rewiring (*51*), in part by repressing *Myc* (*52*), a proto-oncogene that codes for Myc transcription factor and is linked to the up-regulation of the glycolytic pathway in cancer cells (*53*). In the RNA-seq analysis, we observed down-regulation of *Myc* and of *Myc* targets such as genes coding for hexokinase 2 and the key enzyme of glycolysis, namely, the ATP-dependent 6-phosphofructokinase (Pfkp), which catalyzes the first committing step of glycolysis (Fig. 6D). Thus, we investigated the glycolytic function and found a significant decrease in the glycolytic reserve in the cells lacking Kv1.3 (Fig. 6E). This parameter indicates the ability of the cells to respond to an energetic demand and is critical for cell survival in B16F10 cells (*54*). In accordance, total ATP level was reduced significantly in both KD lines (Fig. 6E). A significant down-regulation of most genes involved in purine and pyrimidine metabolism, linked to proliferation and also to the metastatic potential of melanoma (*55*), was also found (Fig. 6F).

A further consideration arising from the RNA-seq analysis is that a substantial overlap (>100 proteins for each clone and 81 hits in common between the two clones) can be found among the transcript levels of differentially expressed genes and the protein partners of Kv1.3 identified by BioID (Fig. 6G). These proteins converge for both clones on translation, RNA binding, cytoskeleton, and Ras GTPase binding (figs. S30 and S31). Altogether, these results indicate that several proteins identified in the Kv1.3 interactome, which are expected to profoundly affect cell behavior, are differentially expressed in the absence of the channel.

Kv1.3 expression is required for melanoma growth and metastasis in vivo

Given these notable differences in vitro, we next established orthotopic melanoma models using both Kv1.3 KD clones and control B16F10 cells. Both KD clones produced notably smaller tumors than parental B16F10 (Fig. 7, A and B). Metastasis to lung was drastically reduced for both Kv1.3 KD B16F10 lines (Fig. 7C).

To investigate the changes in Kv1.3-linked signaling pathways that may underlie such differential growth, we compared the activation of some cancer-related pathways in the B16F10WT and Kv1.3 KD clone-induced primary tumors grown for 15 days. One of the prominent pathways emerging from BioID is the EGFR-linked pathway. To assess whether EGFR activation depends on the presence/activity of Kv1.3 in the tumors, we performed an analysis with

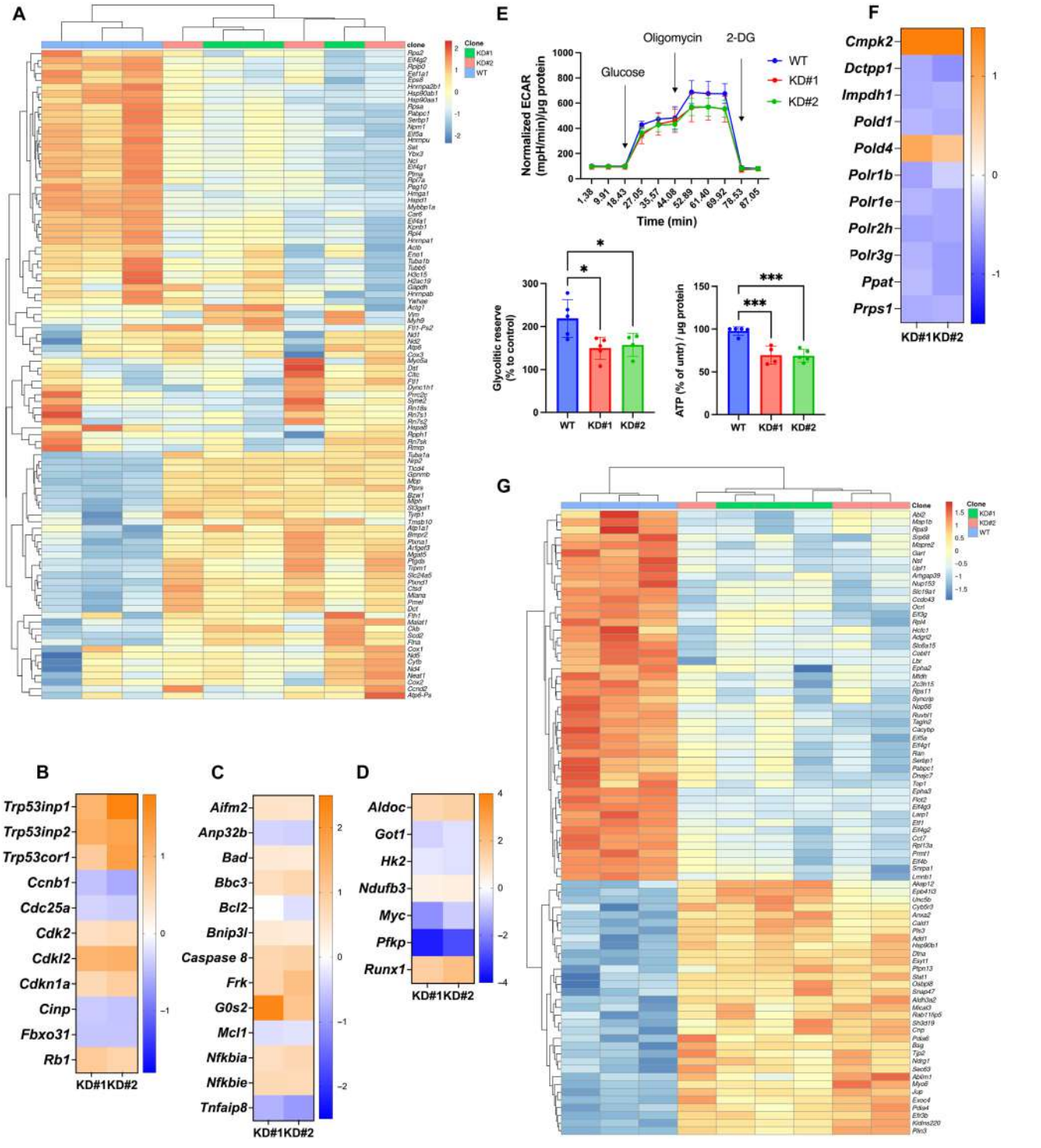

Fig. 6. Gene expression analysis in melanoma cells lacking Kv1.3. (**A**) DEG analysis was performed comparing Kv1.3 KD and WT lines. A total of 2938 and 3524 differentially expressed genes (DEG) compared to WT were found for B16F10 KD Kv1.3 #1 and #2, respectively (FDR < 0.01). Top100 DEGs (with highest SD among all nine samples) are shown for all three replicates per cell line. (**B**) Transcript level of several p53-induced target genes and cell cycle progression regulatory genes. The color key indicates the log2-fold change relative to control in (B) to (D) and (F). (**C**) Transcript level of known pro- and anti-apoptotic players. (**D**) Transcript level of glycolytic genes. (**E**) Measurement of glycolytic capacity, i.e., the rate of increase in ECAR after the injection of oligomycin following glucose addition. Oligomycin inhibits mitochondrial ATP production and therefore shifts the energy production to glycolysis with increase in ECAR revealing maximum glycolytic capacity of the cells. The glycolytic reserve is the difference between glycolytic capacity and glycolysis rate ($n = 3$ independent experiments). (**F**) Transcript level of genes involved in purine and pyrimidine metabolism. (**G**) Heatmap of the transcript levels of 81 DEGs that encode protein partners of Kv1.3 identified by BioID. The shown 81 hits are shared by both clones.

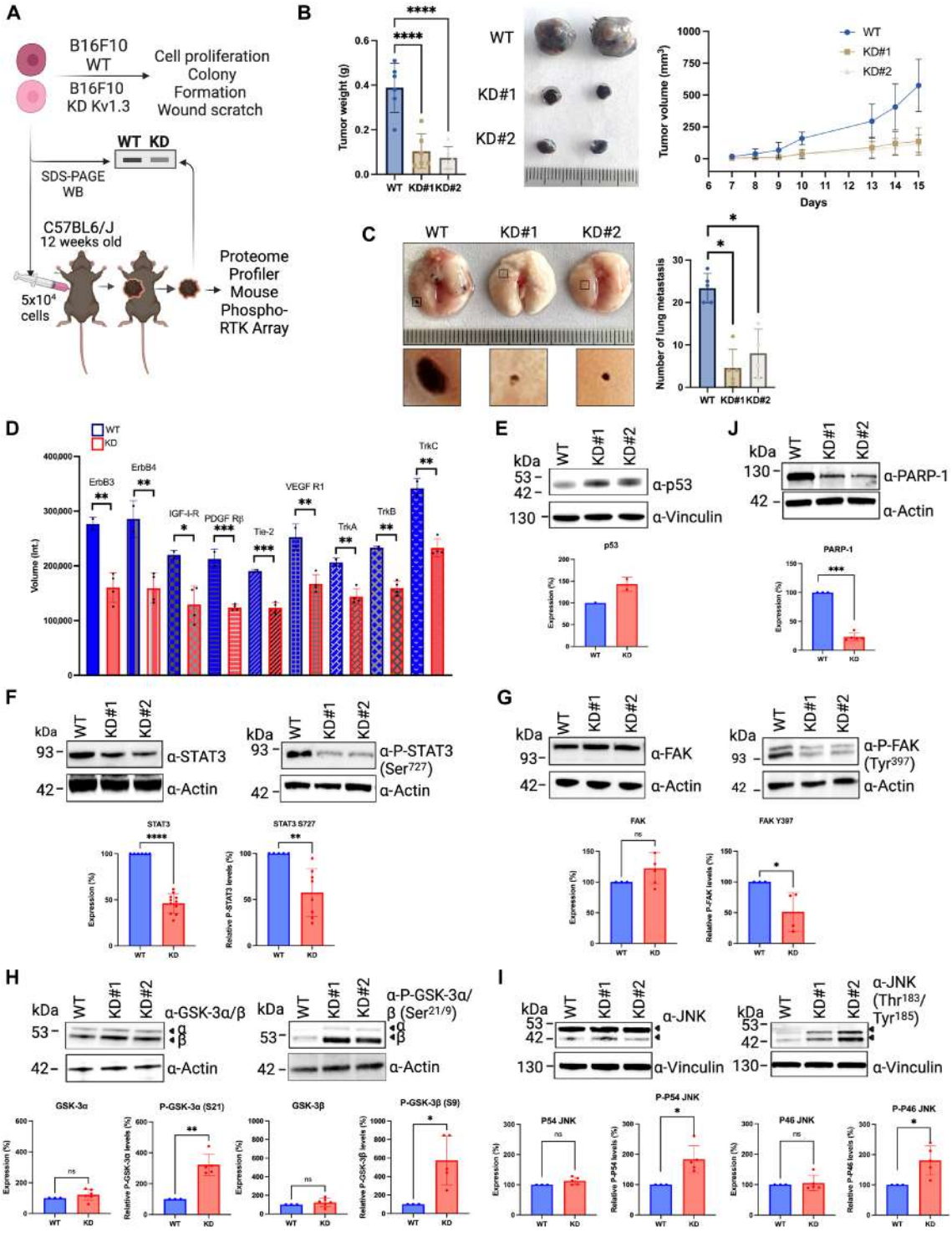

Fig. 7. In vivo tumor growth and metastatic spread in an orthotopic model using WT B16F10 cells and two independent Kv1.3 KD lines. (**A**) Schematic view of the in vivo experiments. (**B**) Six animals from each group were injected with the indicated cell lines. The tumors were excised and are shown in the representative image. Tumor weight and volume are shown. (**C**) Representative photographs of lung metastasis removed after 21 days from the tail vein injection with the indicated cell lines in 9-week-old C57BL6/J mice. Quantification of metastases on the surface of the lung is shown. Data represent mean ± SD. $n = 5$ WT, $n = 5$ KD #1, $n = 4$ KD #2.*$P < 0.05$. (**D**) Phosphorylation array on tumor lysates reveals decreased tyrosine phosphorylation of the indicated proteins in the Kv1.3 KD tumors with respect to WT. Quantification of the dot intensity is shown. (**E** to **J**) SDS-PAGE followed by immunoblotting of B16F10 WT and two Kv1.3 KD clone-derived tumor lysates developed with the indicated antibodies. Quantification was performed on biological ($n = 2$ to 3 for each) and technical replicates ($n \geq 3$ for each).

a mouse phospho-receptor tyrosine kinase profiler (Fig. 7D, fig. S32, and Table 2). We detected reduced activation of EGF receptors Erbb3 and Erbb4 in the B16F10 Kv1.3 KD tumors compared to WT cell-derived tumors (Fig. 7D). Likewise, the phosphorylation of other tyrosine kinase receptors (IGFR1, PDGF Rβ, TkA/B/C, VEGFR, and angiogenesis-promoting Tie-2) also decreased. In accordance with the data of Molhoek *et al.* (*56*), phosphorylation of these receptors was relatively weak in the tumor tissues but was similar to in vitro assay on B16 cells (*57*).

Consistent with the reduced tumor size and confirming the in vitro results, we observed an enhanced stabilization of p53 (Fig. 7E) and a significantly decreased STAT3 level and S727 phosphorylation (Fig. 7F) in the lysates of tumors derived from KD cells. In addition, focal adhesion kinase (FAK) activation/phosphorylation was reduced (Fig. 7G). The phosphorylation of GSK3α/β kinases was instead enhanced in the Kv1.3 KD cell-derived tumors (Fig. 7H). Compatibly with an increased cell death, phosphorylation of the stress kinase JNK at T183 and Y185 increased (Fig. 7I), while total PARP-1 protein levels decreased (Fig. 7J). Altogether, these changes may contribute to the drastically reduced melanoma growth in the absence of Kv1.3.

To understand which pathways maintained the growth of the remnant tumors, we investigated the PI3K/AKT/mammalian target of rapamycin (mTOR) and MAPK/ERK pathways. An increased phosphorylation of ERK 1/2 (fig. S33A) and of AKT at S473 (but not at T308) (fig. S33B) occurred. Likewise, phosphorylation of pRAS40 (fig. S33B) and of mTOR (fig. S33C), downstream targets of AKT, increased in the tumor samples lacking Kv1.3.

DISCUSSION

Here, we analyzed in intact cells the entire systemic interactome of the Kv1.3 ion channel, whose altered expression and function are linked to various diseases. Despite the emerging crucial role of this channel in the context of neurodegenerative, metabolic, and oncologic diseases [for a recent review, see, e.g., (*9*)], the interaction partners that may account for the observed phenotypes upon overexpression or lack of Kv1.3 have not yet been defined at a systemic level. Previous studies have identified that the cytoplasmic domains of Kv1.3 can have roles beyond the regulation of potassium fluxes by participating in some cell signaling pathways, via protein-protein interactions. The proteins known thus far to interact with Kv1.3 are limited to β1-integrin (*58*), cortactin (an SH3 domain–containing F-actin binding protein) (*59*), PDZ family proteins PSD95 and SAP97 (also called disc large 4 and 1, Dlg4 and Dlg1, respectively) (*60*, *61*), and regulatory proteins Kvβ2 and KCNE4 (*62*), as well as caveolin (*63*), Sec24 from COPII (*64*), and calmodulin-binding tetraleucine motif (*65*). We also identified most of these known interactors in our BioID analysis, confirming the validity of the BioID approach but, in addition, revealed a number of unexpected, additional partners. Only a few studies addressed the interactome of ion channels using BioID to date. BioID-identified interactors of another potassium channel, namely, Kir2.1 (*14*)(>200 interactors) and of Kv1.3 only minimally overlap, confirming the specificity of this approach to reliably identify channel interactors.

Here, we focused our attention specifically on the cancer-related pathways emerging from Kv1.3 BioID and validated some of these

Table 2. List of antibodies used in this study.

AKT	Cell Signaling Technology	No. 9272
P-AKT (Ser^{473})	Cell Signaling Technology	No. 4060
P-AKT (Thr^{308})	Cell Signaling Technology	No. 4056
CyclinD1	Cell Signaling Technology	No. 2978
EGFR	Genetex	GTX121919
P-EGFR (Tyr^{1068})	Cell Signaling Technology	No. 3777
FAK	Cell Signaling Technology	No. 3285
P-FAK (Tyr^{397})	Cell Signaling Technology	No. 3283
GFP	Proteintech	50430-2-AP
P-GSK-3α/β (Ser^{21}/Ser^{9})	Cell Signaling Technology	No. 8566
P42/P44 MAPK	Cell Signaling Technology	No. 4695
P-P42/P44 MAPK (Thr^{202}/Tyr^{204})	Cell Signaling Technology	No. 9101
mTOR	Cell Signaling Technology	No. 2972
P-mTOR (Ser^{2448})	Cell Signaling Technology	No. 5536
P-mTOR (Ser^{2481})	Cell Signaling Technology	No. 2974
p53	Cell Signaling Technology	No. 2527
P-p53 (Ser^{392})	Cell Signaling Technology	No. 9281
P-PRAS (Thr^{246})	Cell Signaling Technology	No. 2997
SAPK/JNK	Cell Signaling Technology	No. 9252
PARP	Genetex	GTX100573
P-JNK (Thr^{183}/Tyr^{185})	Genetex	GTX635799
STAT3	Cell Signaling Technology	No. 9139
P-STAT3 (Ser^{727})	Cell Signaling Technology	No. 9134
P-STAT3 (Tyr^{705})	Cell Signaling Technology	No. 9145

results in the newly generated melanoma cell lines lacking the channel, both in vitro and in vivo. Notably, the tumors formed by the Kv1.3-KD melanoma cells were significantly smaller than those formed by the parental control, and metastatic spread to the lungs was drastically reduced. Multiple mechanisms may account for this notable reduction in melanoma growth and migration, including an unexpected physical and functional interaction between Kv1.3 and STAT3 in cancer cells. On the basis of our results as well as those described in the literature regarding the interplay between signaling pathways, we propose that in the absence of Kv1.3, an altered EGFR-integrin signaling leads to inactivation of FAK, with consequent decreased Rho GTPase activity and decreased migration. Inactivated FAK as well as an interaction between Kv1.3/mitoKv1.3 and STAT3 may contribute to decreased STAT3 activity that in turn stabilizes p53. The enhanced mitochondrial ROS in cells lacking Kv1.3 or upon inhibition of the mitochondrial channel with mitochondria-targeted Kv1.3 inhibitors promote activation of JNK that we have previously shown to trigger apoptosis upon mitoKv1.3 inhibition even in vivo (*66*). Stabilized p53 not only contributes to apoptosis induction but also modulates metabolism as well as cell cycle progression and proliferation (Fig. 8).

Recent evidence claims that Kv1.3 contributes to cancer progression by an ion flux–independent mechanism (*16*, *26*), which envisions the channel as a modulator coupling voltage-dependent conformational changes with proliferation signaling and cellular respiration. The molecular details, however, are still unclear, but the epidermal growth factor (EGF)–dependent signaling and Kv1.3 regulation were reported to be tightly related (*67*). Members of the EGF family of structurally related tyrosine kinase receptors, known as the ErbB receptors (EGFR/ErbB1/HER1, ErbB2/HER2/neu, ErbB3/HER3, and ErbB4/HER4) and their respective ligands, have been suggested to be involved in the development and progression of malignant melanoma, and ErbB receptor kinase inhibitors were proposed as a previously unidentified promising treatment strategy in malignant melanoma. In particular, the Erbb3-linked (*68*) and Erbb4-linked (*69*) pathways (both Erbb3 and Erbb4 are down-regulated in Kv1.3 KD tumors, see Fig. 7D) are currently in the focus in the context of melanoma. In addition to EGFR family receptors, TrkA/B/C receptor activation was also reduced in the Kv1.3 KD tumors. Inhibition of these receptors in different melanoma lines prevented proliferation (*70*). Thus, the observed decrease of the tumor volume is compatible with the detected reduction in the phosphorylation-linked activation of various tyrosine kinase receptors.

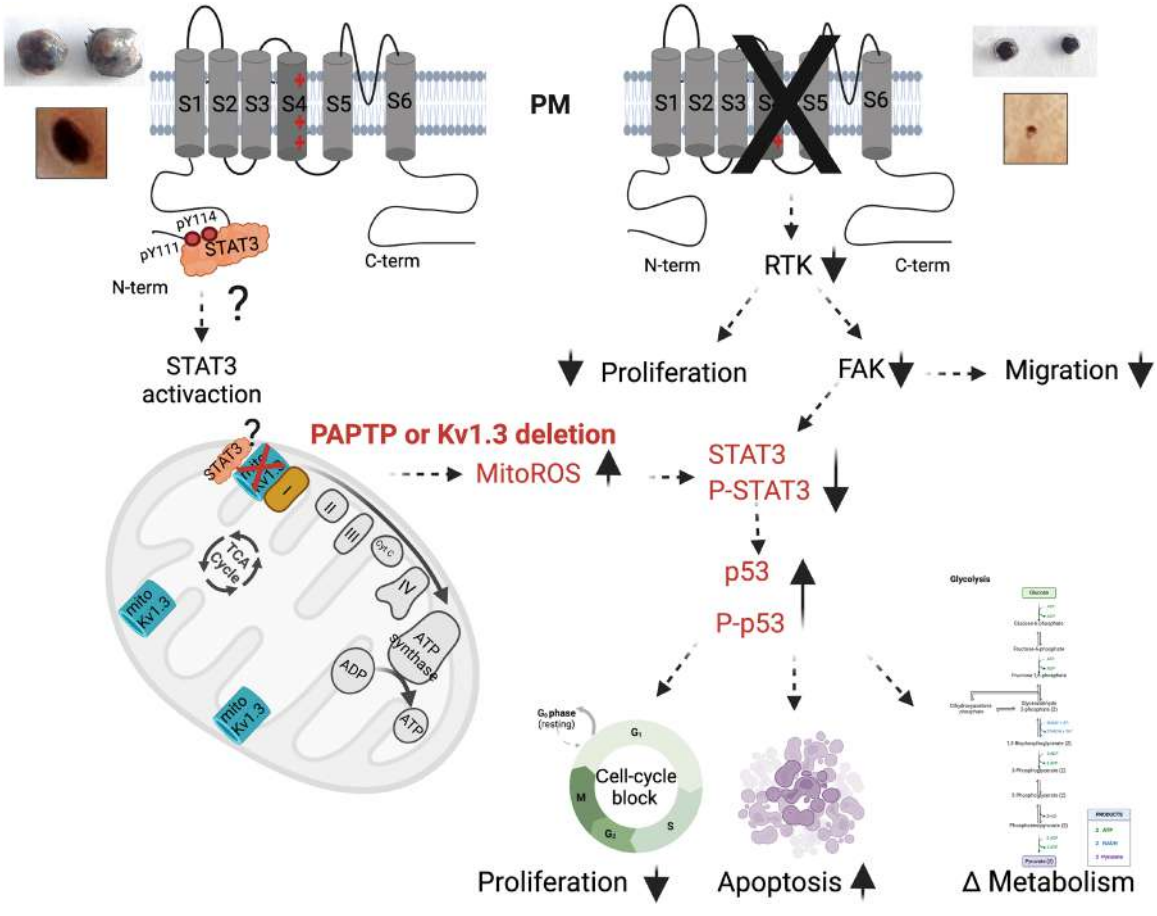

Fig. 8. Cartoon of the proposed mechanisms accounting for reduced tumor growth. Kv1.3 is required for tumor growth as it interacts with STAT3 and promotes its phosphorylation. In addition, lack or inhibition of the mitochondrial Kv1.3 leads to enhanced mitochondrial ROS release and to phosphorylation of p53 at Ser^{392} that promotes its migration to mitochondria and its proapoptotic function. p53 stabilization affects cell cycle, apoptosis, and metabolism. See the Results and Discussion sections for explanation and discussion of further Kv1.3-linked pathways that may contribute to reduced tumor growth in the absence of the channel.

EGFR activation-triggered signaling is known to cross-talk with integrin-mediated signaling (*71*). In melanoma cells, the interaction of Kv1.3 with β1-integrin (confirmed here both by BioID and Myc-Trap coimmunoprecipitation) was shown to be modulated by Kv1.3 inhibitors, suggesting that Kv1.3 blockers might have an impact on cancer cell behavior by affecting the assembly of supramolecular structures containing integrins and possibly other proteins (*72*), although this hypothesis has not been experimentally tested. An important early signal triggered by integrin activation is the phosphorylation and consequent activation of FAK, a cytoplasmic tyrosine kinase considered as integrin adaptor, whose activation correlates with tumor progression. Here, we show that FAK activation, triggered by Y397 phosphorylation, was markedly reduced in both Kv1.3 KD tumors with respect to the WT sample. FAK controls a number of cellular functions, including proliferation, invasion, and epithelial-mesenchymal transition, by activating numerous signaling pathways (*73*). The interaction between Kv channels and integrins might be crucial for FAK activation and tumorigenesis. Rho GTPases, which are downstream of FAK, are central regulators of actin reorganization and consequently affect cellular processes such as cell migration. In our study, we identified several Kv1.3 interactors in focal adhesion as cellular component, and Rho GTPase downstream effectors, such as *Pak3*, were among the top down-regulated transcripts in the RNA-seq analysis in the KD lines compared to the WT cells. These results suggest that similar to another Kv channel, Kv11.1, Kv1.3 might also modulate Rho GTPase activity. Further experiments are required to test this hypothesis. In any case, the role of Kv1.3 for migration both in vitro and in vivo is crucial, as we found that Kv1.3 KD cells gave metastasis to significantly less extent than the WT cells.

Similar to other cancer types, FAK activation strictly correlates with activation of STAT3, a crucial protumorigenic transcription factor and with malignancy progression in melanoma (*73*). STAT3 was among the enriched hits in our BioID analysis, was coimmunoprecipitated with Kv1.3, and interacted with the channel in PLA experiments, suggesting an interaction/physical proximity between the two proteins. Although our docking analysis identified possible regions involved in STAT3-Kv1.3 interaction, the molecular details remain to be dissected. STAT3 has been shown to be present in mitochondria as a consequence of Y705 phosphorylation by JAK, whereas its mitochondrial transcriptional activity and its effect on proliferation depend on the MAPK-mediated phosphorylation of STAT3 at S727 (*74*, *75*). STAT3 can be activated through S727 phosphorylation, even in the absence of pY705. Thus, reduction of S727 and Y705 phosphorylation by the lack of Kv1.3/PAPTP might be relevant to dampen B16F10 proliferation. Our results highlight that modulation of Kv1.3 expression/activity was able to diminish STAT3 phosphorylation and enhance p53 stabilization/phosphorylation not only in murine and human melanoma cells but also in pancreatic ductal adenocarcinoma cells, and even in the presence of mutated p53 in Colo357 and SKMEL28 cells, allowing generalization of the observed mechanism.

In contrast to the pore blockers Shk and Mgtx, the mitoKv1.3 inhibitor PAPTP alone can trigger the above events in a Kv1.3-dependent way in B16F10 cells. We saw the effect of PAPTP on p53 only when STAT3 was not silenced. Although our data indicate a physical and functional interaction between STAT3 and Kv1.3, they suggest that Kv1.3 modulation affects STAT3 phosphorylation also indirectly, through PAPTP- or channel deletion–triggered ROS release. We have previously shown that Kv1.3 deletion triggers mitochondrial fragmentation (*35*) that is typically associated with high ROS production by dysfunctional mitochondria. We observed a higher basal ROS level in both Kv1.3 KD melanoma clones. High ROS release can activate p38MAPK/JNK (c-Jun-N-terminal kinase) (*66*) (JNK activation was observed here in the KD tumors), and the downstream molecules activated or inhibited by JNK include p53 and STAT3, respectively [e.g., (*76*)]. Thus, the here-observed elevated mitochondrial ROS and activation of JNK stress kinase may also contribute to both STAT3 inactivation and p53 stabilization. The relevance of mitochondrial ROS in the latter event is indicated by the fact that incubation of the cells with MITOTEMPO, a scavenger of mitochondrial ROS, prevented the p53 stabilization and its phosphorylation at S392 by PAPTP that triggers mitochondrial ROS release. PAP-1 derivatives were shown to amplify ROS production by inhibiting respiratory chain complex I function, through interaction with a nonpore region of Kv1.3 (*20*). Independently of the molecular details, an increased S392 p53 phosphorylation is associated with mitochondrial translocation and proapoptotic activity of p53 (*44*). In summary, the observed JNK activation, along with the decreased levels of full-length poly(ADP-ribose) polymerase-1 (PARP-1) (*77*) and p53 activation we observed in the KD tumors, likely contributes to enhanced apoptosis and reduced proliferation, leading to smaller tumor volume.

Another factor that might contribute to the reduced growth of Kv1.3-deleted B16F10 tumors is the inactivation of GSK3α and GSK3β (glycogen synthase kinase-3) isoforms by phosphorylation of S21 and S9, respectively. The phosphorylation of both isoforms is generally inhibitory and involves modulation of apoptosis, cell proliferation, and migration. Inhibition of GSK3β was shown to prevent mouse melanoma cell growth in vitro and in vivo (*78*). In summary, the modulation of the above pathways likely accounts for the reduced tumor size obtained using the Kv1.3 KD melanoma lines.

However, the Kv1.3-KD tumors were still able to grow. Therefore, we examined whether activation of resistance pathways such as proliferation-related ERK and AKT/mTOR signaling took place in the small remnant tumors grown under Kv1.3 deficiency. AKT activation promotes melanoma progression (*79*). In our tumor samples, phosphorylation of AKT at S473, within the noncatalytic region, and of the AKT downstream target, the proline-rich AKT substrate of 40 kDa PRAS40—a constituent of mTORC1 (*80*)—at Thr^{246} was enhanced in the absence of the channel. Phosphorylation of PRAS40 is often associated with the tumor progression of melanoma as it promotes tumorigenesis by deregulating cellular proliferation, apoptosis, senescence, and metastasis (*81*). In addition to the activation of the AKT/pRAS40/mTOR pathway, phosphorylated ERK was also enhanced. The importance of aberrant activation of the ERK signaling pathway in tumorigenesis has been demonstrated in more than 80% of cutaneous melanomas (*82*). Thus, activation of these two pathways is most likely responsible for tumor progression in the absence of Kv1.3 and might take part in a compensatory mechanism that counteracts the antiproliferative effects exerted by the lack of Kv1.3. As mentioned in Introduction, pharmacological modulation of Kv1.3 drastically reduced tumor size in different models, although it did not completely eliminate them. Thus, the observations described here might help to set up a combination treatment by counteracting pro-proliferative pathways that remain active when Kv1.3 is absent or inhibited.

Altogether, we explored the interactome of Kv1.3 potassium channel in intact cells, highlighting the participation of Kv1.3 in

unexpected signaling networks. The present work is expected to help to identify the most efficient Kv1.3-based combination treatment(s) to halt tumor progression in vivo and may become a source of useful information also for other cancer types where Kv1.3 crucially contributes to tumor progression. Our study also revealed several so far unidentified links between Kv1.3 and molecular pathways that might be of interest in various fields. For example, a suggested role for Kv1.3 in axon guidance (*83*) and in the bacterial/viral infection response (*84*) deserves further attention. Furthermore, the ability of Kv1.3 to interact with STAT3 (and possibly other members of the family) may importantly affect cell signaling in the context of immune cell function where altered Kv1.3 expression/function is linked to different pathologies, such as autoimmune and neurodegenerative diseases. In this respect, we would like to mention that while our manuscript was under review, the group of Rangaraju and colleagues posted a study on bioRxiv addressing the interactome of Kv1.3 using TurboID and found a PDZ domain–dependent interaction of the channel with STAT1 in microglial cells. In addition, they further confirmed mitochondrial localization of Kv1.3 through the identification of a number of mitochondrial proteins in their TurboID analysis.

MATERIALS AND METHODS

General laboratory chemicals were purchased from Sigma-Aldrich unless otherwise specified.

Plasmid construction

The Kv1.3 coding sequence was PCR amplified from the pEYFP-C1-rKv1.3 using the primer_FOR1 5′-TCCGGACTCGAGTCTATGACCGTG-3′ and the primer_REV1 5′-TTTTATGTTTCAGGTTCAGGGGG-3′. The PCR product was digested by Xho I and Eco RI and inserted into pcDNA3.1 mycBioID (pcDNA3.1 mycBioID was a gift from K. Roux (Addgene plasmid no. 35700; http://n2t.net/addgene:35700; RRID:Addgene_35700). To fuse the Kv1.3 CDS to the N terminus of BirA(R118G), it was PCR amplified from pEYFP-C1-rKv1.3 using primer_FOR2 5′-TCCGGACTCGCTAGCTATGA-CCGTG-3′ and primer_REV2 5′-CTGCAGAATTCGAAGCTATTTTTGACATCAGTG-3′. The PCR product was then digested by Nhe I and Eco RI and ligated into pcDNA3.1 MCS-BirA (R118G)-HA. pcDNA3.1 MCS-BirA(R118G)-HA was a gift from K. Roux (Addgene plasmid no. 36047; http://n2t.net/addgene:36047; RRID:Addgene_36047). The sequences of the final plasmids were confirmed using restriction digestions and DNA sequencing. To generate the mito-YFP-rKv1.3 construct, the mitochondrial targeting sequence of subunit VIII of cytochrome c oxidase amplified from pLV_mitoGFP (Addgene 44385) incorporating Nhe I–Age I restriction sites using Phusion High-Fidelity DNA polymerase (Thermo Fisher Scientific, F-530) was inserted between Nhe I–Age I restriction sites (New England Biolabs, R3131 and R3552, respectively) in YFP-rKv1.3 in pEYFP-C1 construct (from A. Felipe), using T4 Ligase (New England Biolabs, M0202). The construct was verified by sequencing. The following were the primers used: Forward: 5′-ATAGCTAGCATGTCCGTCCTGACGCCGCTGCTGC; Reverse: 5′-AATACCGGTATCTTGGCGCGCGGCACTGGGAGCC.

Cell culture

HEK293 cells were grown in Dulbecco's modified Eagle's medium (DMEM) supplemented with 10% fetal bovine serum (FBS), 10 mM Hepes, penicillin (100 U/ml) and streptomycin (100 U/ml), and 1× nonessential amino acids. B16F10 cells were grown in MEM supplemented with 10% (v/v) FBS, penicillin G (100 U/ml), streptomycin (0.1 mg/ml), 1% nonessential amino acids, 2 mM L-glutamine, and 1 mM sodium pyruvate. All materials for cell culture were purchased from Gibco. Cells were maintained at 37°C and 5% CO_2.

Generation of stable HEK293 cell lines expressing Kv1.3-BirA* constructs

TransIT-LT1 transfection reagent (Mirus) was used to transfect HEK293 cells with plasmids pcDNA 3.1 mycBioID in fusion with *KCNA3* encoding Kv1.3, and pcDNA3.1 MCS-BirA (R118G)–HA in fusion with *KCNA3*. HEK293 cells were incubated overnight and the day after the medium was replaced with fresh DMEM without antibiotics. Reduced serum Opti-MEM I medium (250 μl; Thermo Fisher Scientific) was mixed with 2.5 μg of plasmid DNA. Trans IT-LT1 Reagent was then mixed with the diluted DNA mixture and was added to the cells. After 2 days, geneticin (750 μl/ml; Gibco) was added. When cells reached 80% confluence, they were diluted in a way to obtain single clones.

Membrane protein extraction and Western blot analysis of cultured cells

The soluble and membrane protein fractions were separated and collected using the manufacturer's instructions of ProteoExtract (Merck/Sigma-Aldrich). For Western blot, after washing with phosphate-buffered saline (PBS), detached cells were centrifuged (5 min, 600*g*). Subsequently, cells were lysed in lysis buffer [25 mM tris-HCl, pH 7.8, 2.5 mM EDTA, 10% (v/v) glycerol, and 1% (v/v) NP-40] supplemented with the protein inhibitor cocktail (Sigma-Aldrich) and 2 mM dithiothreitol (DTT). Bradford Assay determined protein concentrations. Equal amounts of proteins dissolved in loading buffer [30% glycerol, 0.313 M tris-HCl (pH 6.8), 9% SDS, 0.1 M DTT, and 0.1% bromophenol blue] were separated by electrophoresis on 4 to 12% ExpressPlus PAGE (polyacrylamide gel electrophoresis) gels (GenScript), under denaturing conditions. Proteins, as indicated, were electro-blotted onto PVDF (polyvinylidene difluoride) membrane (Amersham). After transfer and blocking (10% milk for 1 hour at room temperature), the membrane was incubated with the specific primary antibody at 4°C. After incubation with secondary antibody at room temperature for 1 hour, the membrane was developed with a high-end imaging system for chemiluminescence detection (Chemidoc, Bio-Rad). The following primary antibodies were used: Anti-BirA (1:100; Novus Biologicals), anti-myc (1:1000; Sigma-Aldrich), anti-Kv 1.3 (1:500; Neuromab), streptavidin-HPR (1:40,000; Thermo Fisher Scientific), anti-actin (1:2000; Millipore), and anti-vinculin (1:3000; Sigma-Aldrich; additional antibodies are listed below).

Transfection and protein silencing

For transfection experiments, cells were transfected using Lipofectamine 2000 Transfection Reagent following the manufacturer's instructions. HEK239 cells and B16F10 KD #1 and KD #2 were seeded till reaching 70% of confluence in six-well plates, and the day after, cells were transfected with different YFP-rKv1.3 constructs (Kv1.3-YFP WT, mitoKv1.3-YFP, and pore dead mutant Kv1.3-YFP W386F at different concentrations as indicated in the figures) for 24 hours and then used for experiments. For siRNA experiments, cells were transfected using Lipofectamine RNAiMAX Transfection Reagent following the manufacturer's instructions. A total of 75,000

SKMEL-28 cells were seeded in a six-well plate, and the day after, they were transfected with either 20 nM siRNA Kv1.3(Origene) (SR302508A, Sense: rArCrArArCrArGrArCrUrUrArCrGrUrUrA-rArArCrUrUrCAT, Antisense: rArUrGrArArGrUrUrUrArArCr-GrUrArArGrUrCrUrGrUrUrGrUrUrU; SR302508B, Sense: rArGr-CrArUrUrArGrArCrUrArArCrArGrArUrUrCrCrUrGTG, Anti-sense: rCrArCrArGrGrArArUrCrUrGrUrUrArGrUrCrUrArArUr-GrCrUrUrU) or 20 nM scramble negative control. After 72 hours, cells were lysed for Western blot analyses. In the case of STAT3 silencing experiment, 100,000 B16F10 cells were seeded in a six-well plate and transfected with siRNA STAT3 (Cell Signaling) following the manufacturer's instructions.

Immunofluorescence

Cells were washed with PBS and fixed with 3.8% paraformaldehyde in PBS for 20 min. Cells were then washed with PBS and permeabilized with 0.1% Triton X-100 in PBS for 5 min. After permeabilization and washing three times with PBS, cells were incubated with 2% bovine serum albumin (BSA) for 1 hour at room temperature. Anti-myc (Abcam, 1:500), anti-HA (Abcam, 1:500), and anti-PMCA (Invitrogen, 1:100) were used to identify tagged BirA*-Kv1.3 fusion proteins and biotinylated proteins, respectively. For ROI (region of interest) analysis, B16F10 cells were silenced for HSPH1 as described in the relevant section (see below). Fixed cells were incubated with primary antibodies anti-myc (Abcam, 1:500) and anti-Na^+/K^+ adenosine triphosphatase (ATPase) (1:100, Sigma-Aldrich), anti-TOM20 (1:500, SCBT no. sc-11415), or anti-vinculin (1:400, Sigma-Aldrich no. V9264). Proteins were visualized with goat anti-mouse 488 (Invitrogen, 1:500), goat anti-mouse 568 (Invitrogen, 1:500), goat anti-rabbit 488 (Invitrogen, 1:500), goat anti-rabbit 568 (Invitrogen, 1:500), or streptavidin coupled to Alexa Fluor 488 (Invitrogen, 1:1000). Coverslips were mounted in ProLong Diamond Antifade Mountant with DAPI (4′,6-diamidino-2-phenylindole) (Invitrogen). The images were obtained at 25°C using a Leica SP5 confocal microscope (Leica Microsystem, Wetzlar, Germany). ROI analysis was performed with the ROI manager of the LAS AF Lite program (Science microscope software platform, Leica).

Mitochondrial colocalization

A total of 100,000 cells were seeded on a 13-mm-diameter coverslip in a 24-well plate for 24 hours. Before the experiment, the cells were transfected with Kv1.3YFP and mitoKv1.3YFP, using Lipofectamine 2000 (Thermo Fisher Scientific). After 24 hours, transfection cells were stained with MitoTracker Red CMXRos (Cell Signaling no. 9082) for 30 min in the dark at 37°C and then fixed with 4% paraformaldehyde at room temperature for 15 min and washed three times with PBS.

The slides were then mounted using Mounting Medium. Cells were imaged by placing the slides on the stage of an LSM700 (Zeiss) confocal microscopy equipped with a 63× and 100×, Zeiss Plan-Apochromat 63×-100×/1.4 oil objective and excited using the appropriate laser line (DAPI: 405 nm ex; YFP: 488 nm ex; Mitotracker: 594 nm ex). Images were acquired using a 1048 × 1048 pixel resolution with the ZEN software (Zeiss). Signal colocalization analysis between the YFP channel and the Mitotracker channel was performed with the Mosaic plugin on ImageJ.

Proximity ligation assay

The PLA assay was performed using a Duolink In Situ Red Mouse/Rabbit kit (DUO92101, Sigma-Aldrich) on HEK293 cells and B16F10 KO#1 and KO#2 Kv1.3 KD cells. Briefly, 30,000 cells were seeded on a 13-mm-diameter coverslip in a 24-well plate for 24 hours. Before the experiment, the cells were transfected with Kv1.3YFP, Kv1.3YFP W386F (pore mutation), and mitoKv1.3YFP, using Lipofectamine 2000 (Thermo Fisher Scientific). After 24 hours, transfected cells were fixed with 4% paraformaldehyde at room temperature for 15 min, washed three times with PBS, and then permeabilized with 0.2% Triton-X 100 in PBS for 8 min. Afterward, the blocking step was performed by using 2% BSA in PBS at room temperature for 1 hour. Therefore, coverslips were incubated overnight at 4°C in a humidified chamber together with anti-STAT3 (Cell Signaling, no. 9139) and anti-GFP (Proteintech, 50430-2-AP).

To perform PLA, cells were washed twice with Buffer A (DUO82046, Sigma-Aldrich) for 5 min each at room temperature and then incubated for 1 hour at 37°C with secondary antibodies conjugated with complementary oligonucleotides [anti-rabbit PLUS (DUO82002, Sigma-Aldrich) and anti-mouse MINUS (DUO82004, Sigma-Aldrich)], diluted 1:5 in the Duolink Antibody Diluent (DUO82008, Sigma-Aldrich). After three washes in Buffer A (5 min each, at room temperature), cells were incubated with DNA Ligase (DUO82029, Sigma-Aldrich) properly diluted 1:5 in Ligation Buffer (DUO82009, Sigma-Aldrich) for 30 min at 37°C in a preheated humidified chamber. Subsequently, cells were washed three times in Buffer A (5 min each, at room temperature) and incubated for 100 min at 37°C with DNA Polymerase (DUO82030, Sigma-Aldrich) diluted 1:5 in Amplification Buffer (DUO82011, Sigma-Aldrich) containing red fluorescent-labeled oligonucleotides, for 100 min at 37°C in a preheated humidified chamber and in the dark. Cells were washed with 1× Buffer B (DUO82048) for 10 min and eventually once with 0.01× Buffer B for 1 min protecting them from light. The slides were then mounted using Duolink In Situ Mounting Medium containing DAPI (DUO82040, Sigma-Aldrich). Cells were imaged by placing the slides on the stage of an LSM700 (Zeiss) confocal microscopy equipped with a 63× and 100×, Zeiss Plan-Apochromat 63×-100×/1.4 oil objective and excited using the appropriate laser line (DAPI: 405 nm ex; YFP: 488 nm ex; Duolink: 594 nm ex). Images were acquired using a 1048 × 1048 pixel resolution with the ZEN software (Zeiss).

Determination of ATP concentration in cells

The total ATP amount was measured using the ATPlite Luminescence ATP Detection Assay System (PerkinElmer). A total of 50,000 B16F10 WT and KD #1 and KD #2 were seeded into a 12-well plate in complete culture medium and incubated at 37°C in a humidified atmosphere with 5% CO_2 for 24 hours. Cells were lysed with 200 µl of lysis buffer provided within the above-mentioned kit and 50 µl of the cell lysate was loaded into a white 96-well plate for the measurement in triplicates. The assay was performed according to the manufacturer's instructions and the luminescence was measured with a PerkinElmer EnVision plate reader. The remaining cell lysate amount was used to quantify the protein amount by means of a BCA protein assay kit (A55864, Invitrogen).

Patch clamp

Current conduction by Kv1.3 channels was assessed by recording the whole-cell patch clamp in HEK293 cells. Briefly, whole-cell currents were recorded with an EPC-7 amplifier (List, Darmstadt, Germany; filter, 500 Hz; sampling rate, 5 kHz). The bath solution was composed of 160 mM NaCl, 5 mM KCl, 2.5 mM $CaCl_2$, 1 mM $MgCl_2$, and 10 mM Hepes (pH 7.3). The pipette solution contained 150 mM

KCl, 1 mM $CaCl_2$, 2 mM $MgCl_2$, 10 mM EGTA, and 10 mM Hepes (pH 7.3). Intracellular voltages are reported, and outward currents are plotted. Patch clamp on Jurkat cells was performed as described in (*21*).

Biotinylation analysis

Cells (0.5×10^6) stably expressing the BioID-Kv1.3 fusion proteins (myc-BirA*-Kv1.3 or Kv1.3-BirA*-HA) and control cells expressing the BioID tag alone (myc-BirA* or BirA*-HA) were seeded in a six-well plate. To induce protein biotinylation, cells were cultured in a medium supplemented with 50 μM biotin for 1, 3, 6, 9, or 24 hours. The following day, cells were washed with PBS and resuspended in lysis buffer [25 mM tris-HCl, pH 7.8, 2.5 mM EDTA, 10% (v/v) glycerol, and 1% (v/v) NP-40], supplemented with protease inhibitor cocktail and 2 mM DTT. Cells were collected by centrifugation for 10 min at 20,000*g*, 4°C, and the supernatant was used for immunoblotting.

Biotinylated proteins were loaded onto 4 to 12% ExpressPlus PAGE gels (GenScript) and transferred to nitrocellulose membranes (Amersham Protran). The membranes were blocked 30 min in 1% BSA in PBS with 0.2% Triton X-100 and incubated 40 min in the same buffer with HRP-conjugated streptavidin (Thermo Fisher Scientific, 1:40,000). After three washes in PBS for 10 min, the membranes were incubated in a luminol and peroxide solution (in a 1:1 ratio) (Bio-Rad) for 5 min. The reaction was detected with a high-end imaging system for chemiluminescence detection (Chemidoc, Bio-Rad).

BioID pull-down

HEK293 (1×10^6) cells stably expressing the BioID-Kv1.3 fusion proteins (myc-BirA*-Kv1.3 or Kv1.3-BirA*-HA) and control cells expressing the BioID tag alone (myc-BirA* or BirA*-HA) were seeded in four 10-cm plates. To induce protein biotinylation, 48 hours after the seeding, 50 μM biotin was added to media for 24 hours. The day after, cells were washed with PBS, collected and lysed with RIPA lysis buffer [50 mM tris-HCl, pH 7.5, 150 mM NaCl, 1 mM EDTA, 1% (v/v) NP-40, 0.1% (w/v) SDS, 0.5% (w/v) sodium deoxycholate, and 1 mM DTT, supplemented with protease inhibitors], and incubated on ice for 15 min. Cells were collected by centrifugation for 10 min at 13,000*g*, 4°C and the supernatant was used for streptavidin-based pull-down using MyOne Dynabeads Streptavidin C1 (Thermo Fisher Scientific) as described previously (*24*). Biotinylated proteins were detected by SDS-PAGE and immunoblotting as described above for biotinylated proteins. Western blot or mass spectroscopy was performed to identify biotinylated proteins.

Coimmunoprecipitation

For the experiments reported in table S2, HEK293 (1×10^6) cells stably expressing the myc-BirA*-Kv1.3 BioID-Kv1.3 fusion proteins and control cells expressing the BioID myc-tag alone were seeded. After 48 hours, cells were collected and lysed in 10 mM tris-HCl, pH 7.5, 150 mM NaCl, 0.5 mM Na-EDTA, and 0.5% NP-40, supplemented with protease inhibitors and 1 mM PMSF. Proteins were coimmunoprecipitated using Nano-Traps (ChromoTek Myc-Trap) using the manufacturer's instructions and proteins were identified by MS ($n = 3$). For coimmunoprecipitation, B16F10 KD cells were transfected with Kv1.3-YFP. Twenty-four hours after transfection, cells were harvested with NP-40 lysis buffer supplemented with protease inhibitors and centrifuged for 15 min at 15,000*g*. The supernatant was then incubated with Dynabeads Protein G (Thermo Fisher Scientific) conjugated with either GFP or STAT3 antibody, with gentle rocking overnight at 4°C. The next day, the sample was washed three times with cold PBS. Bound proteins were then eluted with 30 μl of elution buffer, denatured with 3× SDS sample buffer, and boiled for 10 min at 95°C before SDS-PAGE Western blot analysis.

Mass spectrometry

Sample preparation SP3 and TMT labeling, OASIS

The reduction of disulfide bridges in cysteine-containing proteins was performed with DTT (56°C, 30 min, 10 mM in 50 mM Hepes, pH 8.5). Reduced cysteines were alkylated with 2-chloroacetamide (room temperature, in the dark, 30 min, 20 mM in 50 mM Hepes, pH 8.5). Samples were prepared using the SP3 protocol (*85*) and trypsin (sequencing grade, Promega) was added in an enzyme-to-protein ratio of 1:50 for overnight digestion at 37°C. The peptides were labeled with TMT11plex (*28*) Isobaric Label Reagent (Thermo Fisher Scientific) according to the manufacturer's instructions. Samples were combined for the TMT11plex, and for further sample cleanup, an OASIS HLB μElution Plate (Waters) was used. Offline high-pH reverse-phase fractionation was carried out on an Agilent 1200 Infinity high-performance liquid chromatography system, equipped with a Gemini C18 column (3 μm, 110 Å, 100 × 1.0 mm, Phenomenex).

LC-MS/MS acquisition

An UltiMate 3000 RSLC nano-LC system (Dionex) fitted with a trapping cartridge (μ-Precolumn C18 PepMap 100, 5 μm, 300 μm i.d. × 5 mm, 100 Å) and an analytical column (nanoEase M/Z HSS T3 column 75 μm × 250 mm C18, 1.8 μm, 100 Å, Waters) were used. The trapping was carried out with a constant flow of trapping solution (0.05% trifluoroacetic acid in water) at 30 μl/min onto the trapping column for 6 min. Subsequently, the peptides were eluted via analytical column running solvent A [0.1% formic acid in water and 3% dimethyl sulfoxide (DMSO)] with a constant flow of 0.3 μl/min, with an increasing percentage of solvent B (0.1% formic acid in acetonitrile, 3% DMSO). The outlet of the analytical column was coupled directly to an Orbitrap Fusion Lumos Tribrid Mass Spectrometer (Thermo) using the Nanospray Flex ion source in positive ion mode.

The peptides were introduced into the Fusion Lumos via a PicoTip Emitter 360 μm OD × 20 μm ID, 10 μm tip (New Objective), and an applied spray voltage of 2.4 kV. The capillary temperature was set at 275°C. The full mass scan was acquired with mass ranges of 375 to 1500 mass/charge ratio (m/z) in profile mode in the orbitrap with a resolution of 120,000. The filling time was set at a maximum of 50 ms with a limitation of 4×10^5 ions. Data-dependent acquisition was performed with the resolution of the Orbitrap set to 30,000, with a fill time of 94 ms and a limitation of 1×10^5 ions. A normalized collision energy of 38 was applied. The MS2 data were acquired in profile mode.

MS data analysis—IsobarQuant

IsobarQuant and Mascot (v2.2.07) were used to process the acquired data, which were searched against a UniProt *Homo sapiens* proteome database (UP000005640) containing common contaminants and reversed sequences. The following modifications were included in the search parameters: carbamidomethyl (C) and TMT11 (K) (fixed modification), acetyl (protein N-terminal), oxidation (M), and TMT11 (N-terminal) (variable modifications). For the full scan (MS1), a mass error tolerance of 10 parts per million was set and for an MS/MS (MS2) spectra of 0.02 Da. Further parameters were established: trypsin as protease with an allowance of a maximum of two missed cleavages:

a minimum peptide length of seven amino acids; at least two unique peptides were required for protein identification. The FDR at the peptide and protein level was set to 0.01.

MS data analysis

The raw IsobarQuant output files (protein.txt–files) were processed using the R programming language (www.r-project.org). Only proteins that were quantified with at least two unique peptides and identified in all mass spec runs were considered for analysis. Raw reporter ion intensities (signal_sum columns) were first cleaned for batch effects using limma (*86*) and further normalized using vsn (variance stabilization normalization) (*87*). Missing values were imputed with the "knn" method using the Msnbase package (*88*). The differential expression of the proteins was tested using the limma package. The replicate information was added as a factor in the design matrix given as an argument for the limma lmFit function. Furthermore, the imputed values were given a weight of 0.05 in the "lmFit" function. A protein was annotated as a hit with an FDR smaller than 5% and a fold change of at least 100% (twofold change).

Bioinformatic analysis

The list of the selected proteins was used to identify significantly enriched functional categories. Enrichment analyses were performed using the clusterProfiler R package (*89*) on GO categories of biological processes, molecular function, and cellular component as well as Reactome and KEGG pathway databases (*90*). FDR was used to control for multiple testing. A threshold of 0.01 (FDR < 0.01) was used to identify significantly enriched GO terms, while 0.1 (FDR < 0.1) was used for Reactome and KEGG pathways. Semantic similarity distance as implemented in the rrvo R package (https://ssayols.github.io/rrvgo) was implemented to reduce redundancy of the significant GO terms. Dot plots, scatterplots, and treeplots were used to graphically summarize and report the results. Maps of the significantly enriched KEGG pathways were colored according to the logarithmic fold change (log2FC) of the proteins.

Deletion of the Kv1.3 gene in B16F10 cells using CRISPR-Cas9

The CRISPR-Cas9 approach followed the guidelines described by Ran *et al.* (*91*) using pSpCas9n (BB)-2A-Puro (PX459) (Addgene Plasmid no. 48139 Zhang Lab). The sgRNA guides were designed to excise the whole and only exon of *KCNA3* (Mm*KCNA3*_u5: GCGGCGGGGCCGGGCTCGTAGGG; Mm*KCNA3*_u6: TGGCGGCAGCTCGGCGTGGCCGG; Mm*KCNA3*d_10: CATTTCCAGACCACTCATCAAGG). Single guides were ligated into the vector at the Bbs I (NEB) restriction site under the U6 promoter and verified by sequencing. Different couples of single guides were used to transfect cells B16 F10 using 1.25 μg of plasmid DNA for each guide with TransIT-LT1 transfection reagent (Mirus). Puromycin (2.5 μg/ml; Gibco) was added to the cell culture medium 48 hours after transfection and kept for 96 hours.

After selection, cells were serially diluted to obtain single-cell clones. Clones were expanded and cells were collected by centrifugation for 5 min at 600*g*. After removing the media, DNA was extracted from the pellet using the MyTaq Extract-PCR kit (Meriadin Bioscience) following the manufacturer's instructions and quantified. A control PCR was performed with the following primers: *kcna3*_F1 rev: CTGCTGGGAAGACTTGAGACC; *kcna3*_R2b for: TGAGAGAATGCAGCCCACTTG.

To test Kv1.3 expression in WT versus KD clones, 300,000 cells were seeded in six-well plates. Two days after seeding, total RNA was extracted using the Qiagen RNeasy Mini Kit (Qiagen, no. 74104). Genomic DNA was digested following the manufacturer's instructions. RNA (3 μg) was retrotranscribed using the SuperScript IV Reverse Transcriptase (Thermo Fisher Scientific, no. 18091050) following the manufacturer's instructions. cDNA was diluted and amplified in qRT-PCR using SYBR Green PCR Master Mix (Thermo Fisher Scientific, no. 4309155). TATA-box binding protein (Tbp) was used as housekeeping control. CT values were first normalized with respect to the housekeeping genes (ΔCT) and next compared to the control sample (ΔΔCT). This relative normalized expression is indicated in fig. S19A. The primers used for amplification are shown in Table 1.

RNA-seq analyses: Alignment, preprocessing, and differential expression

Total RNA was isolated from B16F10 cells using the RNeasy Mini Kit (Qiagen) following the manufacturer's instructions. Each group contains three biological replicates. Reads were aligned to the reference genome with STAR (v 2.7.10a) (*92*) and quantified with RSEM (v1.3.1). The indexed genome was built with RSEM starting from Ensembl's *Mus musculus* DNA primary assembly (release 106) (*93*). For all of the nine aligned samples, we obtained a percentage of uniquely mapped reads between 70% and 75%, while the numbers of uniquely mapped reads were between 27,000,000 and 43,000,000.

After the quantification, data were filtered, keeping only genes with at least 20 counts in three different samples.

To identify the differentially expressed genes, we used the edgeR R package (*94*). We provided as input the filtered raw counts with the design matrix defined by the dichotomous variables for the different clones. The RLE normalization was applied to the samples. An FDR of less than 0.01 was used to select significantly differentially expressed genes (DEGs). BioProject accession number is PRJNA902542.

DEGs were used to perform enrichment analysis (separately for up- and down-regulated genes) on KEGG, GO, and Reactome databases with clusterProfiler and ReactomePA R packages. For the enrichment analysis, the universe was set as the list of the genes with at least one count in one sample. An adjusted *P* value of less than 0.1 was used to select significant gene sets and pathways. Cluster analysis was performed using the pheatmap R package with the complete linkage method with Euclidean distances.

Wound scratch assay

A total of 35,000 B16 F10 cells per well were seeded in a 24-well plate in standard culture medium and allowed to grow for 48 hours. The scratch was performed with a sterile p200 pipette tip. The medium was removed and substituted with serum- and phenol red-free medium. Images of the same fields were taken 0, 15, 20, and 24 hours after scratching with a Leica DMI4000 inverted microscope. The scratch area was calculated using the ImageJ software (NIH Bethesda, MD). The migration rate is expressed as a percentage of the initial gap area. For rescue experiments, cells were treated with Rho/Rac/Cdc42 Activator I (2.5 μg/ml, Cytoskeleton Inc. no. CN-04°) after having performed the scratch. The inhibitor was present throughout the assay.

Proliferation and colony formation assay

To assess cell proliferation, 15,000 B16 F10 cells were seeded in 12-well plates in standard culture medium. Cells were detached with

trypsin at 24, 48, 36, and 72 hours and diluted in 100 µl of medium. Cells were counted using LUNAII Automated Cell counter (Logos Biosystem). For colony formation, 500 B16 F10 were seeded in a six-well plate and allowed to grow for 6 days in standard culture medium. The medium was removed, and cells were washed twice with PBS and fixed with 3.8% paraformaldehyde for 30 min. After three washes with PBS, cells were stained with 0.1% crystal violet for 15 min at room temperature and washed with PBS until colonies cleared. Images were taken with Leica MZ stereo microscope16 F with 1× 0.5 magnification. The number and dimension of colonies were quantified with ImageJ software.

Measurement of extracellular acidification rate

The XFe24 Extracellular Flux Analyzer (SeaHorse) was used to measure the extracellular acidification rate (ECAR). A total of 22,000 B16F10 cells were seeded in standard culture medium and incubated for 24 hours at 37°C. The medium was then replaced with white DMEM without glucose and sodium pyruvate. ECAR was measured with preset time intervals upon the automated additions of the following compounds: 5 mM glucose, oligomycin (2 µg/ml), and 40 mM 2-DG. ECAR was normalized to the total protein.

Determination of mitochondrial ROS release

B16F10 WT and Kv1.3-KD clones were subjected to staining with MitoSOX at a concentration of 2.5 µM for 30 min at 37°C. The stained cells were analyzed using a Fortessa flow cytometer (Becton Dickinson). Analyses were performed with FlowJo software.

Orthotopic and metastatic B16 F10 melanoma model

WT mice (12 weeks old) in the C57BL6/J background were kept on a 12-hour light/dark cycle at controlled temperature and humidity, with standard food (4RF21, Mucedola Srl, Italy) and water provided ad libitum and environmental enrichments. Subconfluent WT murine melanoma B16F10 and clones B16F10 Kv1.3 KD #1 and #2 were trypsinized, washed, and resuspended in PBS. Cell suspension (5×10^4 cells in 100 µl of PBS) was injected subcutaneously into the right flank of each mouse. Equal numbers of females and males were used and animals were chosen randomly for the injection with the indicated cell lines. The tumor growth of WT and KD clones was assessed by measuring the length and width of each tumor every day and calculating the tumor volume using the following formula: (tumor volume = length × width)]^2 × 0.5. Fifteen days after tumor cell injection, the mice were euthanized, and their tumors were harvested.

Subconfluent B16F10 WT, KD #1, and KD #2 cells were trypsinized, washed, and resuspended in PBS. Cell suspensions of B16F10 WT, KD #1, and KD #2 (2×10^5 cells in 100 µl PBS) were injected into the tail vein of 9-week-old WT C57BL/6J mice. After 3 weeks after injection, the mice were euthanized, and the lungs were perfused with 10 ml of PBS through the right ventricle of the heart. The lungs were then removed, and colonies were counted with the aid of a dissecting microscope.

Mouse phospho-RTK (receptor tyrosine kinase) proteome profiler array and Western blot

The tumors were excised from mice and lysed in 25 mM tris-HCl, pH 7.8, 2.5 mM EDTA, 10% (v/v) glycerol, and 1% (v/v) NP-40 supplemented with protease and phosphatase inhibitor cocktail and 2 mM DTT and broken with Qiagen TissueLyser II sample disruption. The total amount of proteins obtained was measured with the Bradford assay. Proteins (200 µg) were used for the assay. The samples (tumors derived from parental B16F10 and B16F10 Kv1.3 KD #1 and #2) were treated using the manufacturer's recommended protocol of Proteome Profiler Array (Mouse phospho-array kit, R&D Systems). The membranes were incubated in a luminol and peroxide solution (in a 1:1 ratio) (Bio-Rad) for 5 min. The reaction was detected with a high-end imaging system for chemiluminescence detection (Chemidoc, Bio-Rad). Images were analyzed with ImageJ software. For classical Western blots, tissues were lysed in 25 mM tris-HCl, pH 7.8, 2.5 mM EDTA, 10% (v/v) glycerol, and 1% (v/v) NP-40, supplemented with protease inhibitor cocktail and 2 mM DTT, loaded onto SDS-PAGE and blotted with the primary antibodies listed in Table 2. In Fig. 5 (D and E), the membrane was cut into 3 pieces: the upper part of the membrane was developed using an anti-vinculin antibody (detecting the 130-kDa band of vinculin) and is therefore shown as loading control for the other two parts of the blot that were developed with antibodies detecting STAT3/pSTAT3 (72 kDa) or p53/p-p53 (53 kDa), respectively. In Fig. 5E, the second piece of the membrane was first developed with anti-pSTAT3 Ser^{727} and after re-stripping with anti-pSTAT3 Tyr^{705}.

Ethics statement

Animal experiments were carried out according to the Local Ethics Committee of the University of Padua and the National Agency and under the supervision of the Central Veterinary Service of the University of Padova (in compliance with Italian law DL 116/92 and further modifications, embodying UE directive 86/609), authorization no. 111/2017-PR.

Statistical analysis

All statistical analyses were performed with the GraphPad Prism 8 software. Three or more groups were analyzed with one-way analysis of variance (ANOVA). Two-way ANOVA was used for parametric data, and Kruskal-Wallis test was used for nonparametric data. Two-way ANOVA with Bonferroni's test was used to compare the data with two variables. Unpaired, Student's *t* test was used to compare two groups. Additional statistical details can be found in the figure legends.

Supplementary Materials

This PDF file includes:

Figs. S1 to S33
Tables S1 to S5

REFERENCES AND NOTES

1. L. A. Pardo, W. Stuhmer, The roles of K^+ channels in cancer. *Nat. Rev. Cancer* **14**, 39–48 (2014).
2. A. Lee, B. Fakler, L. K. Kaczmarek, L. L. Isom, More than a pore: Ion channel signaling complexes. *J. Neurosci.* **34**, 15159–15169 (2014).
3. M. Perez-Verdaguer, J. Capera, C. Serrano-Novillo, I. Estadella, D. Sastre, A. Felipe, The voltage-gated potassium channel Kv1.3 is a promising multitherapeutic target against human pathologies. *Expert Opin. Ther. Targets* **20**, 577–591 (2016).
4. S. Sarkar, H. M. Nguyen, E. Malovic, J. Luo, M. Langley, B. N. Palanisamy, N. Singh, S. Manne, M. Neal, M. Gabrielle, A. Abdalla, P. Anantharam, D. Rokad, N. Panicker, V. Singh, M. Ay, A. Charli, D. Harischandra, L. W. Jin, H. Jin, S. Rangaraju, V. Anantharam, H. Wulff, A. G. Kanthasamy, Kv1.3 modulates neuroinflammation and neurodegeneration in Parkinson's disease. *J. Clin. Invest.* **130**, 4195–4212 (2020).
5. C. Beeton, H. Wulff, N. E. Standifer, P. Azam, K. M. Mullen, M. W. Pennington, A. Kolski-Andreaco, E. Wei, A. Grino, D. R. Counts, P. H. Wang, C. J. LeeHealey, B. S. Andrews, A. Sankaranarayanan, D. Homerick, W. W. Roeck, J. Tehranzadeh, K. L. Stanhope, P. Zimin, P. J. Havel, S. Griffey, H. G. Knaus, G. T. Nepom, G. A. Gutman,

P. A. Calabresi, K. G. Chandy, Kv1.3 channels are a therapeutic target for T cell-mediated autoimmune diseases. *Proc. Natl. Acad. Sci. U.S.A* **103**, 17414–17419 (2006).
6. S. Bittner, S. G. Meuth, Targeting ion channels for the treatment of autoimmune neuroinflammation. *Ther. Adv. Neurol. Disord.* **6**, 322–336 (2013).
7. M. Bachmann, W. Li, M. J. Edwards, S. A. Ahmad, S. Patel, I. Szabo, E. Gulbins, Voltage-gated potassium channels as regulators of cell death. *Front Cell Dev Biol* **8**, 611853 (2020).
8. A. Teisseyre, A. Palko-Labuz, K. Sroda-Pomianek, K. Michalak, Voltage-Gated Potassium Channel Kv1.3 as a Target in Therapy of Cancer. *Front. Oncol.* **9**, 933 (2019).
9. T. Varanita, B. Angi, V. Scattolini, I. Szabo, Kv1.3 K^+ channel physiology assessed by genetic and pharmacological modulation. *Physiology (Bethesda)* **38**, 25–41 (2022).
10. K. J. Roux, D. I. Kim, B. Burke, D. G. May, BioID: A screen for protein-protein interactions. *Curr. Protoc. Protein Sci.* **91**, 19.23.1–19.23.15 (2018).
11. K. J. Roux, D. I. Kim, M. Raida, B. Burke, A promiscuous biotin ligase fusion protein identifies proximal and interacting proteins in mammalian cells. *J. Cell Biol.* **196**, 801–810 (2012).
12. M. Iazzi, A. Astori, J. St-Germain, B. Raught, G. D. Gupta, Proximity profiling of the CFTR interaction landscape in response to Orkambi. *Int. J. Mol. Sci.* **23**, 2442 (2022).
13. E. Kaikkonen, A. Takala, J. P. Pursiheimo, G. Wahlström, J. Schleutker, The interactome of the prostate-specific protein Anoctamin 7. *Cancer Biomark* **28**, 91–100 (2020).
14. S. S. Park, D. Ponce-Balbuena, R. Kuick, G. Guerrero-Serna, J. Yoon, D. Mellacheruvu, K. P. Conlon, V. Basrur, A. I. Nesvizhskii, J. Jalife, J. F. Rual, Kir2.1 interactome mapping uncovers PKP4 as a modulator of the Kir2.1-regulated inward rectifier potassium currents. *Mol. Cell. Proteomics.* **19**, 1436–1449 (2020).
15. T. Bergermann, L. Born, F. Ferguson, P. Latkovic, A. Scheul, N. Sonnenschein, L. Leanza, S. Keitsch, C. Sehl, B. Wilker, M. J. Edwards, M. Zoratti, C. Paradisi, M. Kohnen, I. Szabo, K. A. Becker, A. Carpinteiro, Inhibition of PI-3-K and AKT amplifies Kv1.3 inhibitor-induced death of human T leukemia cells. *Cell. Physiol. Biochem.* **53**, 1–10 (2019).
16. L. Jimenez-Perez, P. Cidad, I. Alvarez-Miguel, A. Santos-Hipolito, R. Torres-Merino, E. Alonso, M. A. de la Fuente, J. R. Lopez-Lopez, M. T. Perez-Garcia, Molecular determinants of Kv1.3 potassium channels-induced proliferation. *J. Biol. Chem.* **291**, 3569–3580 (2016).
17. I. Szabo, J. Bock, A. Jekle, M. Soddemann, C. Adams, F. Lang, M. Zoratti, E. Gulbins, A novel potassium channel in lymphocyte mitochondria. *J. Biol. Chem.* **280**, 12790–12798 (2005).
18. J. Capera, M. Navarro-Pérez, A. S. Moen, I. Szabó, A. Felipe, The mitochondrial routing of the Kv1.3 channel. *Fronti. Oncol.* **12**, 865686 (2022).
19. J. Capera, M. Pérez-Verdaguer, R. Peruzzo, M. Navarro-Pérez, J. Martínez-Pinna, A. Alberola-Die, A. Morales, L. Leanza, I. Szabó, A. Felipe, A novel mitochondrial Kv1.3-caveolin axis controls cell survival and apoptosis. *eLife* **10**, e69099 (2021).
20. R. Peruzzo, A. Mattarei, M. Azzolini, K. A. Becker-Flegler, M. Romio, G. Rigoni, A. Carrer, L. Biasutto, S. Parrasia, S. Kadow, A. Managò, A. Urbani, A. Rossa, G. Semenzato, M. E. Soriano, L. Trentin, S. Ahmad, M. Edwards, E. Gulbins, C. Paradisi, M. Zoratti, L. Leanza, I. Szabò, Insight into the mechanism of cytotoxicity of membrane-permeant psoralenic Kv1.3 channel inhibitors by chemical dissection of a novel member of the family. *Redox Biol.* **37**, 101705 (2020).
21. I. Szabo, J. Bock, H. Grassme, M. Soddemann, B. Wilker, F. Lang, M. Zoratti, E. Gulbins, Mitochondrial potassium channel Kv1.3 mediates Bax-induced apoptosis in lymphocytes. *Proc. Natl. Acad. Sci. U.S.A.* **105**, 14861–14866 (2008).
22. A. Arcangeli, A. Becchetti, Novel perspectives in cancer therapy: Targeting ion channels. *Drug Resist. Updat.* **21**, 11–19 (2015).
23. B. Angi, S. Muccioli, I. Szabò, L. Leanza, A meta-analysis study to infer voltage-gated K^+ channels prognostic value in different cancer types. *Antioxidants* **12**, 573 (2023).
24. V. Le Sage, A. Cinti, A. J. Mouland, Proximity-dependent biotinylation for identification of interacting proteins. *Curr. Protoc. Cell Biol.* **73**, 17.19.11–17.19.12 (2016).
25. R. M. Sears, D. G. May, K. J. Roux, BioID as a tool for protein-proximity labeling in living cells. *Methods Mol. Biol.* **2012**, 299–313 (2019).
26. F. L. Styles, M. M. Al-Owais, J. L. Scragg, E. Chuntharpursat-Bon, N. T. Hettiarachchi, J. D. Lippiat, A. Minard, R. S. Bon, K. Porter, P. Sukumar, C. Peers, L. D. Roberts, Kv1.3 voltage-gated potassium channels link cellular respiration to proliferation through a non-conducting mechanism. *Cell Death Dis.* **12**, 372 (2021).
27. A. Sueki, F. Stein, M. M. Savitski, J. Selkrig, A. Typas, Systematic localization of *Escherichia coli* membrane proteins. *mSystems* **5**, e00808–e00819 (2020).
28. T. Werner, G. Sweetman, M. F. Savitski, T. Mathieson, M. Bantscheff, M. M. Savitski, Ion coalescence of neutron encoded TMT 10-plex reporter ions. *Anal. Chem.* **86**, 3594–3601 (2014).
29. S. E. Calvo, K. R. Clauser, V. K. Mootha, MitoCarta2.0: An updated inventory of mammalian mitochondrial proteins. *Nucleic Acids Res.* **44**, D1251–D1257 (2016).
30. L. Leanza, B. Henry, N. Sassi, M. Zoratti, K. G. Chandy, E. Gulbins, I. Szabo, Inhibitors of mitochondrial Kv1.3 channels induce Bax/Bak-independent death of cancer cells. *EMBO Mol. Med.* **4**, 577–593 (2012).
31. Y. Wang, D. Li, J. Lu, L. Chen, S. Zhang, W. Qi, W. Li, H. Xu, Long noncoding RNA TTN-AS1 facilitates tumorigenesis and metastasis by maintaining TTN expression in skin cutaneous melanoma. *Cell Death Dis.* **11**, 664 (2020).
32. D. Pan, A. Kobayashi, P. Jiang, L. Ferrari de Andrade, R. E. Tay, A. M. Luoma, D. Tsoucas, X. Qiu, K. Lim, P. Rao, H. W. Long, G. C. Yuan, J. Doench, M. Brown, X. S. Liu, K. W. Wucherpfennig, A major chromatin regulator determines resistance of tumor cells to T cell-mediated killing. *Science* **359**, 770–775 (2018).
33. A. Ishibashi, K. Saga, Y. Hisatomi, Y. Li, Y. Kaneda, K. Nimura, A simple method using CRISPR-Cas9 to knock-out genes in murine cancerous cell lines. *Sci. Rep.* **10**, 22345 (2020).
34. A. M. Lopez-Guerrero, C. Pascual-Caro, F. J. Martin-Romero, E. Pozo-Guisado, Store-operated calcium entry is dispensable for the activation of ERK1/2 pathway in prostate cancer cells. *Cell. Signal.* **40**, 44–52 (2017).
35. J. Capera, M. Pérez-Verdaguer, M. Navarro-Pérez, A. Felipe, Kv1.3 controls mitochondrial dynamics during cell cycle progression. *Cancer* **13**, 4457 (2021).
36. J. H. Seo, E. Agarwal, Y. C. Chae, Y. G. Lee, D. S. Garlick, A. M. Storaci, S. Ferrero, G. Gaudioso, U. Gianelli, V. Vaira, D. C. Altieri, Mitochondrial fission factor is a novel Myc-dependent regulator of mitochondrial permeability in cancer. *EBioMedicine* **48**, 353–363 (2019).
37. H. C. Pal, R. Prasad, S. K. Katiyar, Cryptolepine inhibits melanoma cell growth through coordinated changes in mitochondrial biogenesis, dynamics and metabolic tumor suppressor AMPKα1/2-LKB1. *Sci. Rep* **7**, 1498 (2017).
38. A. Schwab, A. Fabian, P. J. Hanley, C. Stock, Role of ion channels and transporters in cell migration. *Physiol. Rev.* **92**, 1865–1913 (2012).
39. R. Berzaghi, V. S. Maia, F. V. Pereira, F. M. Melo, M. S. Guedes, C. S. Origassa, J. B. Scutti, A. L. Matsuo, N. O. Câmara, E. G. Rodrigues, L. R. Travassos, SOCS1 favors the epithelial-mesenchymal transition in melanoma, promotes tumor progression and prevents antitumor immunity by PD-L1 expression. *Sci. Rep.* **7**, 40585 (2017).
40. L. Leanza, M. Romio, K. A. Becker, M. Azzolini, L. Trentin, A. Manago, E. Venturini, A. Zaccagnino, A. Mattarei, L. Carraretto, A. Urbani, S. Kadow, L. Biasutto, V. Martini, F. Severin, R. Peruzzo, V. Trimarco, J. H. Egberts, C. Hauser, A. Visentin, G. Semenzato, H. Kalthoff, M. Zoratti, E. Gulbins, C. Paradisi, I. Szabo, Direct pharmacological targeting of a mitochondrial ion channel selectively kills tumor cells in vivo. *Cancer Cell* **31**, 516–531. e10 (2017).
41. A. Zaccagnino, A. Manago, L. Leanza, A. Gontarewitz, B. Linder, M. Azzolini, L. Biasutto, M. Zoratti, R. Peruzzo, K. Legler, A. Trauzold, H. Kalthoff, I. Szabo, Tumor-reducing effect of the clinically used drug clofazimine in a SCID mouse model of pancreatic ductal adenocarcinoma. *Oncotarget* **8**, 38276–38293 (2017).
42. L. Guo, J. S. Kang, N. J. Kang, Y. W. Choi, S-petasin induces apoptosis and inhibits cell migration through activation of p53 pathway signaling in melanoma B16F10 cells and A375 cells. *Arch. Biochem. Biophys.* **692**, 108519 (2020).
43. V. K. Kashyap, N. Dan, N. Chauhan, Q. Wang, S. Setua, P. K. B. Nagesh, S. Malik, V. Batra, M. M. Yallapu, D. D. Miller, W. Li, B. B. Hafeez, M. Jaggi, S. C. Chauhan, VERU-111 suppresses tumor growth and metastatic phenotypes of cervical cancer cells through the activation of p53 signaling pathway. *Cancer Lett.* **470**, 64–74 (2020).
44. C. Castrogiovanni, B. Waterschoot, O. De Backer, P. Dumont, Serine 392 phosphorylation modulates p53 mitochondrial translocation and transcription-independent apoptosis. *Cell Death Differ.* **25**, 190–203 (2018).
45. K. Sakaguchi, H. Sakamoto, M. S. Lewis, C. W. Anderson, J. W. Erickson, E. Appella, D. Xie, Phosphorylation of serine 392 stabilizes the tetramer formation of tumor suppressor protein p53. *Biochemistry* **36**, 10117–10124 (1997).
46. P. Morlacchi, F. M. Robertson, J. Klostergaard, J. S. McMurray, Targeting SH2 domains in breast cancer. *Future Med. Chem.* **6**, 1909–1926 (2014).
47. M. Wiederkehr-Adam, P. Ernst, K. Müller, E. Bieck, F. O. Gombert, J. Ottl, P. Graff, F. Grossmüller, M. H. Heim, Characterization of phosphopeptide motifs specific for the Src homology 2 domains of signal transducer and activator of transcription 1 (STAT1) and STAT3. *J. Biol. Chem.* **278**, 16117–16128 (2003).
48. J. S. McMurray, Structural basis for the binding of high affinity phosphopeptides to Stat3. *Biopolymers* **90**, 69–79 (2008).
49. M. Remmert, A. Biegert, A. Hauser, J. Söding, HHblits: Lightning-fast iterative protein sequence searching by HMM-HMM alignment. *Nat. Methods* **9**, 173–175 (2011).
50. L. Bai, H. Zhou, R. Xu, Y. Zhao, K. Chinnaswamy, D. McEachern, J. Chen, C. Y. Yang, Z. Liu, M. Wang, L. Liu, H. Jiang, B. Wen, P. Kumar, J. L. Meagher, D. Sun, J. A. Stuckey, S. Wang, A potent and selective small-molecule degrader of STAT3 achieves complete tumor regression in vivo. *Cancer Cell* **36**, 498–511.e17 (2019).
51. Y. Liu, W. Gu, The complexity of p53-mediated metabolic regulation in tumor suppression. *Semin. Cancer Biol.* **85**, 4–32 (2022).
52. M. Sachdeva, S. Zhu, F. Wu, H. Wu, V. Walia, S. Kumar, R. Elble, K. Watabe, Y. Y. Mo, p53 represses c-Myc through induction of the tumor suppressor miR-145. *Proc. Natl. Acad. Sci. U.S.A.* **106**, 3207–3212 (2009).
53. E. S. Goetzman, E. V. Prochownik, The role for Myc in coordinating glycolysis, oxidative phosphorylation, glutaminolysis, and fatty acid metabolism in normal and neoplastic tissues. *Front. Endocrinol.* **9**, 129 (2018).
54. Y. Sugiyama, T. Shudo, S. Hosokawa, A. Watanabe, M. Nakano, A. Kakizuka, Emodin, as a mitochondrial uncoupler, induces strong decreases in adenosine triphosphate (ATP) levels and proliferation of B16F10 cells, owing to their poor glycolytic reserve. *Genes Cells* **24**, 569–584 (2019).

55. M. Kosmopoulou, A. F. Giannopoulou, A. Iliou, D. Benaki, A. Panagiotakis, A. D. Velentzas, E. G. Konstantakou, I. S. Papassideri, E. Mikros, D. J. Stravopodis, E. Gikas, Human melanoma-cell metabolic profiling: Identification of novel biomarkers indicating metastasis. *Int. J. Mol. Sci.* **21**, 2436 (2020).
56. K. R. Molhoek, A. L. Shada, M. Smolkin, S. Chowbina, J. Papin, D. L. Brautigan, C. L. Slingluff Jr., Comprehensive analysis of receptor tyrosine kinase activation in human melanomas reveals autocrine signaling through IGF-1R. *Melanoma Res.* **21**, 274–284 (2011).
57. Y. Hayashi, T. Kawakubo-Yasukochi, A. Mizokami, M. Hazekawa, T. Yakura, M. Naito, H. Takeuchi, S. Nakamura, M. Hirata, Uncarboxylated osteocalcin induces antitumor immunity against mouse melanoma cell growth. *J. Cancer* **8**, 2478–2486 (2017).
58. M. Levite, L. Cahalon, A. Peretz, R. Hershkoviz, A. Sobko, A. Ariel, R. Desai, B. Attali, O. Lider, Extracellular K^+ and opening of voltage-gated potassium channels activate T cell integrin function: Physical and functional association between Kv1.3 channels and beta1 integrins. *J. Exp. Med.* **191**, 1167–1176 (2000).
59. P. Hajdu, G. V. Martin, A. A. Chimote, O. Szilagyi, K. Takimoto, L. Conforti, The C-terminus SH3-binding domain of Kv1.3 is required for the actin-mediated immobilization of the channel via cortactin. *Mol. Biol. Cell* **26**, 1640–1651 (2015).
60. D. R. Marks, D. A. Fadool, Post-synaptic density perturbs insulin-induced Kv1.3 channel modulation via a clustering mechanism involving the SH_3 domain. *J. Neurochem.* **103**, 1608–1627 (2007).
61. O. Szilagyi, A. Boratko, G. Panyi, P. Hajdu, The role of PSD-95 in the rearrangement of Kv1.3 channels to the immunological synapse. *Pflugers Archi.* **465**, 1341–1353 (2013).
62. L. Solé, M. Roura-Ferrer, M. Pérez-Verdaguer, A. Oliveras, M. Calvo, J. M. Fernández-Fernández, A. Felipe, KCNE4 suppresses Kv1.3 currents by modulating trafficking, surface expression and channel gating. *J. Cell Sci.* **122**, 3738–3748 (2009).
63. M. Pérez-Verdaguer, J. Capera, R. Martínez-Mármol, M. Camps, N. Comes, M. M. Tamkun, A. Felipe, Caveolin interaction governs Kv1.3 lipid raft targeting. *Sci. Rep.* **6**, 22453 (2016).
64. R. Martínez-Mármol, M. Pérez-Verdaguer, S. R. Roig, A. Vallejo-Gracia, P. Gotsi, A. Serrano-Albarrás, M. I. Bahamonde, A. Ferrer-Montiel, G. Fernández-Ballester, N. Comes, A. Felipe, A non-canonical di-acidic signal at the C-terminus of Kv1.3 determines anterograde trafficking and surface expression. *J. Cell Sci.* **126**, 5681–5691 (2013).
65. L. Solé, S. R. Roig, D. Sastre, A. Vallejo-Gracia, A. Serrano-Albarrás, A. Ferrer-Montiel, G. Fernández-Ballester, M. M. Tamkun, A. Felipe, The calmodulin-binding tetraleucine motif of KCNE4 is responsible for association with Kv1.3. *FASEB J* . **33**, 8263–8279 (2019).
66. W. Li, G. C. Wilson, M. Bachmann, J. Wang, A. Mattarei, C. Paradisi, M. J. Edwards, I. Szabo, E. Gulbins, S. A. Ahmad, S. H. Patel, Inhibition of a mitochondrial potassium channel in combination with gemcitabine and abraxane drastically reduces pancreatic ductal adenocarcinoma in an immunocompetent orthotopic murine model. *Cancer* **14**, 2618 (2022).
67. R. Martínez-Mármol, N. Comes, K. Styrczewska, M. Pérez-Verdaguer, R. Vicente, L. Pujadas, E. Soriano, A. Sorkin, A. Felipe, Unconventional EGF-induced ERK1/2-mediated Kv1.3 endocytosis. *Cell. Mol. Life Sci.* **73**, 1515–1528 (2016).
68. C. F. Ruggiero, D. Malpicci, L. Fattore, G. Madonna, V. Vanella, D. Mallardo, D. Liguoro, V. Salvati, M. Capone, B. Bedogni, P. A. Ascierto, R. Mancini, G. Ciliberto, ErbB3 phosphorylation as central event in adaptive resistance to targeted therapy in metastatic melanoma: Early detection in ctcs during therapy and insights into regulation by autocrine neuregulin. *Cancer* **11**, 1425 (2019).
69. R. L. Cullum, L. M. Lucas, J. I. Senfeld, J. T. Piazza, L. T. Neel, K. Whig, L. Zhai, M. H. Harris, C. C. Rael, D. C. Taylor, L. J. Cook, D. P. Kaufmann, C. P. Mill, M. A. Jacobi, F. T. Smith, M. Suto, R. Bostwick, R. B. Gupta, A. E. David, D. J. Riese II, Development and application of high-throughput screens for the discovery of compounds that disrupt ErbB4 signaling: Candidate cancer therapeutics. *PLOS ONE* **15**, e0243901 (2020).
70. F. Truzzi, A. Marconi, R. Lotti, K. Dallaglio, L. E. French, B. L. Hempstead, C. Pincelli, Neurotrophins and their receptors stimulate melanoma cell proliferation and migration. *J. Invest. Dermatol.* **128**, 2031–2040 (2008).
71. S. Javadi, M. Zhiani, M. A. Mousavi, M. Fathi, Crosstalk between epidermal growth factor receptors (EGFR) and integrins in resistance to EGFR tyrosine kinase inhibitors (TKIs) in solid tumors. *Eur. J. Cell Biol.* **99**, 151083 (2020).
72. V. V. Artym, H. R. Petty, Molecular proximity of Kv1.3 voltage-gated potassium channels and β_1-integrins on the plasma membrane of melanoma cells: Effects of cell adherence and channel blockers. *J. Gen. Physiol.* **120**, 29–37 (2002).
73. F. J. Sulzmaier, C. Jean, D. D. Schlaepfer, FAK in cancer: Mechanistic findings and clinical applications. *Nat. Rev. Cancer* **14**, 598–610 (2014).
74. M. Peron, A. Dinarello, G. Meneghetti, L. Martorano, R. M. Betto, N. Facchinello, A. Tesoriere, N. Tiso, G. Martello, F. Argenton, Y705 and S727 are required for the mitochondrial import and transcriptional activities of STAT3, and for regulation of stem cell proliferation. *Development* **148**, dev199477 (2021).
75. M. Diallo, F. Herrera, The role of understudied post-translational modifications for the behavior and function of signal transducer and activator of transcription 3. *FEBS J.* **289**, 6235–6255 (2021).
76. D. Gobelli, P. Serrano-Lorenzo, M. J. Esteban-Amo, J. Serna, M. T. Pérez-García, A. Orduña, A. A. Jourdain, M. Á. Martín-Casanueva, M. Á. de la Fuente, M. Simarro, The mitochondrial succinate dehydrogenase complex controls the STAT3-IL-10 pathway in inflammatory macrophages. *iScience* **26**, 107473 (2023).
77. L. Yang, K. Huang, X. Li, M. Du, X. Kang, X. Luo, L. Gao, C. Wang, Y. Zhang, C. Zhang, Q. Tong, K. Huang, F. Zhang, D. Huang, Identification of poly(ADP-ribose) polymerase-1 as a cell cycle regulator through modulating Sp1 mediated transcription in human hepatoma cells. *PLOS ONE* **8**, e82872 (2013).
78. J. D. Kubic, J. B. Mascarenhas, T. Iizuka, D. Wolfgeher, D. Lang, GSK-3 promotes cell survival, growth, and PAX3 levels in human melanoma cells. *Mol. Cancer Res.* **10**, 1065–1076 (2012).
79. G. P. Robertson, Functional and therapeutic significance of Akt deregulation in malignant melanoma. *Cancer Metastasis Rev.* **24**, 273–285 (2005).
80. D. Lv, L. Guo, T. Zhang, L. Huang, PRAS40 signaling in tumor. *Oncotarget* **8**, 69076–69085 (2017).
81. S. V. Madhunapantula, A. Sharma, G. P. Robertson, PRAS40 deregulates apoptosis in malignant melanoma. *Cancer Res.* **67**, 3626–3636 (2007).
82. L. Zhang, S. Meng, B. Yan, J. Chen, L. Zhou, L. Shan, Y. Wang, Anti-proliferative, pro-apoptotic, anti-migrative and tumor-inhibitory effects and pleiotropic mechanism of theaflavin on B16F10 melanoma cells. *Onco. Targets Ther.* **14**, 1291–1304 (2021).
83. S. McFarlane, N. S. Pollock, A role for voltage-gated potassium channels in the outgrowth of retinal axons in the developing visual system. *Neuroscience* **20**, 1020–1029 (2000).
84. Y. Lang, F. Li, Q. Liu, Z. Xia, Z. Ji, J. Hu, Y. Cheng, M. Gao, F. Sun, B. Shen, C. Xie, W. Yi, Y. Wu, J. Yao, Z. Cao, The Kv1.3 ion channel acts as a host factor restricting viral entry. *Exp. Biol.* **35**, e20995 (2021).
85. C. S. Hughes, S. Foehr, D. A. Garfield, E. E. Furlong, L. M. Steinmetz, J. Krijgsveld, Ultrasensitive proteome analysis using paramagnetic bead technology. *Mol. Syst. Biol.* **10**, 757 (2014).
86. M. E. Ritchie, B. Phipson, D. Wu, Y. Hu, C. W. Law, W. Shi, G. K. Smyth, *limma* powers differential expression analyses for RNA-sequencing and microarray studies. *Nucleic Acids Res.* **43**, e47 (2015).
87. W. Huber, A. von Heydebreck, H. Sültmann, A. Poustka, M. Vingron, Variance stabilization applied to microarray data calibration and to the quantification of differential expression. *Bioinformatics* **18**, S96–S104 (2002).
88. L. Gatto, K. S. Lilley, MSnbase—An R/Bioconductor package for isobaric tagged mass spectrometry data visualization, processing and quantitation. *Bioinformatics* **28**, 288–289 (2012).
89. T. Wu, E. Hu, S. Xu, M. Chen, P. Guo, Z. Dai, T. Feng, L. Zhou, W. Tang, L. Zhan, X. Fu, S. Liu, X. Bo, G. Yu, clusterProfiler 4.0: A universal enrichment tool for interpreting omics data. *Innovation* **2**, 100141 (2021).
90. M. Kanehisa, S. Goto, KEGG: Kyoto Encyclopedia of Genes and Genomes. *Nucleic Acids Res.* **28**, 27–30 (2000).
91. F. A. Ran, P. D. Hsu, J. Wright, V. Agarwala, D. A. Scott, F. Zhang, Genome engineering using the CRISPR-Cas9 system. *Nat. Protoc.* **8**, 2281–2308 (2013).
92. A. Dobin, C. A. Davis, F. Schlesinger, J. Drenkow, C. Zaleski, S. Jha, P. Batut, M. Chaisson, T. R. Gingeras, STAR: Ultrafast universal RNA-seq aligner. *Bioinformatics* **29**, 15–21 (2013).
93. B. Li, C. N. Dewey, RSEM: Accurate transcript quantification from RNA-Seq data with or without a reference genome. *BMC Bioinformatics* **12**, 323 (2011).
94. M. D. Robinson, D. J. McCarthy, G. K. Smyth, edgeR: A Bioconductor package for differential expression analysis of digital gene expression data. *Bioinformatics* **26**, 139–140 (2010).
95. R. H. Spencer, Y. Sokolov, H. Li, B. Takenaka, A. J. Milici, J. Aiyar, A. Nguyen, H. Park, B. K. Jap, J. E. Hall, G. A. Gutman, K. G. Chandy, Purification, visualization, and biophysical characterization of Kv1.3 tetramers. *J. Biol. Chem.* **272**, 2389–2395 (1997).

Acknowledgments: We thank G. Hajnoczky and M. Zoratti for the critical reading of the manuscript, M. El Boustani for help with the FACS (fluorescence-activated cell sorting) analysis of the Mitosox signal, V. Brillo for help with silencing, J. Capera for the pore-dead Kv1.3 construct, M. Putnik for help with Western blots, and A. Mattarei for synthesis of PAPTP. We acknowledge American Journal Experts for language editing and the Imaging Facility at the Department of Biology of the University of Padua. **Funding:** We are grateful to the Italian Association for Cancer Research (IG Grant IG 20286 to I.S.) for financial support and to the National Center for Gene Therapy and Drugs Based on RNA Technology, funded in the framework of the National Recovery and Resilience Plan (PNRR-CN3), Mission 4, Component 2, Investment 1.4, funded by the European Union—Next Generation EU, Project CN00000041, CUP C93C22002780006, CN3, Spoke n.2, Cancer (I.S. and L.L.). I.S. and E.G. also thank World Wide Cancer Research WWCR (grant number 22-0348) for financial support. I.S. is also grateful for a Progetti di Rilevante Interesse Nazionale (PRIN) grant from the Ministry of the University, Italy (20174TB8KW_004), to the Italian Association for Multiple Sclerosis (2022/R-single/046), and to the pHIoniC International Training Network for support. V.Ch. expresses gratitude for the financial support received from SEED-PRID project 2021, the Integrated Budget for Interdepartmental Research 2023 (BIRD-PRID, grant number BIRD239198/23), the Project of

National Interest Research 2022 (PRIN, grant number 2022ZY7ATN), and the research project sponsored by Fondazione Cassa di Risparmio di Padova e Rovigo—Scientific Excellence Research Grant 2021. M.B. and L.M.T. are recipients of AIRC fellowships (ID 25364 and ID 29773). L.L. thanks AIRC for MFAG Grant (ID 23271 project) and T.V. is grateful for the STARS project of the University of Padova. **Author contributions:** E.P.: Conceptualization, methodology, investigation, writing—original draft, writing—review and editing, validation, formal analysis, and visualization. V.Ca.: Conceptualization, methodology, investigation, writing—original draft, writing—review and editing, validation, formal analysis, and visualization. L.M.T.: Investigation, writing—review and editing, validation, methodology, formal analysis, and visualization. T.V.: Investigation. M.B.: Investigation. M.F.: Conceptualization, methodology, investigation, writing—original draft, writing—review and editing, validation, formal analysis, and visualization. D.B.: Methodology, investigation, writing—review and editing, and validation. M.P.-V.: Writing—original draft, methodology, investigation, validation, and visualization. A.C.: Investigation, software, formal analysis, and visualization. A.V.: Formal analysis and software. R.P.: Conceptualization, investigation, and writing—review and editing. S.M.: Conceptualization, methodology, resources, and formal analysis. D.D.: Investigation, validation, and visualization. L.L.: Methodology, investigation, writing—original draft, writing—review and editing, validation, and formal analysis. P.C.: Writing—review and editing, resources, and validation. F.S.: Formal analysis and visualization. M.R.: Resources and validation. A.F.: Writing—original draft, conceptualization, writing—review and editing, resources, supervision, and visualization. M.J.E.: Conceptualization, investigation, funding acquisition, supervision, and project management. E.G.: Conceptualization, writing—original draft, writing—review and editing, investigation, funding acquisition, methodology, validation, supervision, and project management. L.C.: Conceptualization, writing—original draft, writing—review and editing, investigation, funding acquisition, methodology, resources, validation, formal analysis, visualization. C.R.: Writing—review and editing, validation, supervision, formal analysis, and software. V.Ch.: Conceptualization, writing—original draft, writing—review and editing, investigation, funding acquisition, methodology, validation, supervision, and project management, resources, formal analysis, and visualization. I.S.: Conceptualization, writing—original draft, writing—review and editing, funding acquisition, methodology, validation, supervision, project management, formal analysis, and visualization. All authors read, edited, and approved the final manuscript. **Competing interests:** The authors declare that they have no competing interests. **Data and materials availability:** All data needed to evaluate the conclusions in the paper are present in the paper and/or the Supplementary Materials.

Submitted 14 January 2024
Accepted 29 July 2024
Published 4 September 2024
10.1126/sciadv.adn9361